PHYSICAL REVIEW D **105,** 074501 (2022)

Proton decay matrix elements on the lattice at physical pion mass

Jun-Sik Yoo,[1,2] Yasumichi Aoki,[3] Peter Boyle,[4,5] Taku Izubuchi,[4,6] Amarjit Soni,[4] and Sergey Syritsyn[1,6]
[1]*Department of Physics and Astronomy, Stony Brook University, Stony Brook, New York 11794, USA*
[2]*Theory Center, Institute of Particle and Nuclear Studies, High Energy Accelerator Research Organization (KEK), Tsukuba 305-0801, Japan*
[3]*RIKEN Center for Computational Science, Kobe 650-0047, Japan*
[4]*Physics Department, Brookhaven National Laboratory, Upton, New York 11973, USA*
[5]*University of Edinburgh, Edinburgh EH9 3JZ, Scotland, United Kingdom*
[6]*RIKEN-BNL Research Center, Brookhaven National Lab, Upton, New York 11973, USA*

(Received 15 November 2021; accepted 7 March 2022; published 8 April 2022)

Proton decay is a major prediction of grand-unified theories (GUT) and its observation would indicate baryon number violation that is required for baryogenesis. Many decades of searching for proton decay have constrained its rate and ruled out some of the simplest GUT models. Apart from the baryon number-violating interactions, this rate also depends on transition amplitudes between the protons and mesons or leptons produced in the decay, which are matrix elements of three-quark operators. We report the nonperturbative calculation of these matrix elements for the most studied two-body decay channels into a meson and antilepton done on a lattice with physical light and strange quark masses and lattice spacings $a \approx 0.14$ fm and 0.20 fm. We perform nonperturbative renormalization and excited state analysis to control associated systematic effects. Our results largely agree with previous lattice calculations done with heavier quark masses and thus remove ambiguity in ruling out some simple GUT theories due to quark mass dependence of hadron structure.

DOI: 10.1103/PhysRevD.105.074501

I. INTRODUCTION

Proton decay is a $|\Delta B| = 1$ baryon number-violating process that has been predicted by grand-unified theories (GUT) [1–3] but has not been observed so far. The Standard Model Lagrangian does not contain baryon number-violating interactions, and although sphaleron processes can convert baryons into antileptons, such transitions are highly suppressed at temperatures below the electroweak phase transition [4,5]. Discovery of proton decay may potentially fulfil one of the three prerequisites to explain the baryon asymmetry in the Universe [6],[1] and also demand extension of the Standard Model to accommodate baryon number violation [8], potentially involving supersymmetry [9,10].

There have been several experiments aimed at observing proton decay: KOLAR [11], NUSEX [12], Frejus [13], SOUDAN [14], Kamiokande [15], IMB [16], and Super Kamiokande [17]. The most recent experiment, Super Kamiokande, has been operating for more than two decades and has set proton partial-lifetime limits $\tau/\mathrm{Br}(p \to e^+\pi^0) \geq 1.6 \times 10^{34}$ years [17] and $\tau/\mathrm{Br}(p \to \nu K^+) \geq 5.9 \times 10^{33}$ years [18]. The next generation of experiments to look for decay of the proton, DUNE [19] and Hyper Kamiokande [20], are expected to start observation in 2024 and 2027, respectively, and to improve these limits by roughly an order of magnitude. Hyper-Kamiokande is a water Cherenkov detector and is best suited to constrain the pion decay mode; it will improve the bound on $\tau/\mathrm{Br}(p \to e^+\pi^0)$ to $\gtrsim 10^{35}$ in 8 years of operation (4 Mt*year exposure) [21]. DUNE, a LArTPC detector, is expected to produce the best limit on the kaon decay mode $\tau/\mathrm{Br}(p \to \bar{\nu}K) \gtrsim 6 \times 10^{34}$ years [22] in two decades of running. JUNO is another neutrino experiment to be installed in China [23]. It is a 20 kt liquid scintillator (LS) detector buried 700 m under a granite mountain, which can detect proton decays in the $p \to K^+\bar{\nu}$ channel. First it detects K^+ decay with kinetic energy of 105 MeV from proton decay, and then it traces the subsequent μ decay. With an efficiency of 64% and the background of 0.5 event per 20 kt year, it can reach a sensitivity of 1.9×10^{34} years in 10 years of operation.

Grand unified theories [1–3] and supersymmetric grand unified theories (SUSY-GUTs) [24–26] hypothesize the existence of larger gauge groups that unify all the

---

[1] There are viable alternatives such as leptogenesis [7].

interactions at some energy scale $\Lambda_{\mathrm{GUT}} \approx 10^{16}$ GeV that may lead to effective quark-lepton interactions causing the proton to decay. At the hadronic scale, these effective interactions are the lowest, dimension-six operators comprised of four fermion fields [27,28],

$$\mathcal{L}_{\mathrm{eff}} = \sum_I C_I \mathcal{O}_I + \mathrm{H.c.},$$
$$\mathcal{O}_I = \epsilon^{abc}(\bar{q}^{aC} P_{\chi_I} q^b)(\bar{\ell}^C P_{\chi'_I} q^c), \tag{1}$$

where $\{\bar{q}, \bar{\ell}\}^C = \{q, \ell\}^T C$ are charge-conjugated fields,^{2} and the chirality projectors are $P_{\chi^{(\prime)}=R,L} = \frac{1\pm\gamma_5}{2}$. The interacting quark fields $q = u$, d, s and the Wilson coefficients C_I depend on the character and the scale of an underlying unified theory. In the simplest case, such an interaction describes proton decay into a lepton and one or more mesons. Neglecting for now the lepton mass $m_{\bar{\ell}} \ll m_N$, the partial decay width of the channel $p \to \Pi\bar{\ell}$ is equal to

$$\Gamma(p \to \Pi\bar{\ell}) = \frac{m_N}{32\pi}\left[1 - \left(\frac{m_\Pi}{m_N}\right)^2\right]^2 \left|\sum_I C_I W^I_{\bar{\ell}}\right|^2, \tag{2}$$

where the meson states are $\Pi = \pi$, K, the final leptons are $\bar{\ell} = e^+, \bar{\nu}, \mu^+$, and the $W_{\bar{\ell}}$ are the $p \to \Pi$ transition matrix elements of the quark component of the operators $\mathcal{O}_I$ (1), which are classified below. The decay rates are determined by effective interactions induced by particular GUT hypotheses at scale $\Lambda_{(\mathrm{GUT})}$ and encoded in the Wilson coefficients $C_I = \frac{\tilde{c}_I}{\Lambda^2}$, where $\tilde{c}_I$ is a dimensionless $O(1)$ coupling renormalized to the nuclear scale. However, the hadronic matrix elements $\langle \Pi\ell|\mathcal{O}_I|p\rangle$ are determined by nonberturbative quark dynamics and have to be evaluated either in a model or, preferably, in an *ab initio* QCD calculation. From dimensional analysis, $W^I_\ell \propto \Lambda^2_{\mathrm{QCD}}$ and the proton decay rate is suppressed as $\Gamma \propto m_N |c_I|^2 (\Lambda_{\mathrm{QCD}}/\Lambda_{(\mathrm{GUT})})^4 \propto \Lambda^5_{\mathrm{QCD}}/m^4_X$ where m_X is the mass of a unified-theory boson. Using $\Lambda_{\mathrm{QCD}} = 0.2$ GeV yields a reasonable estimate for the form factors value $|W_{\bar{\ell}}| \approx 0.04\ \mathrm{GeV}^2$ and an estimate for the partial lifetime

$$\tau/\mathrm{Br}(p \to \pi\bar{\ell}) \approx 1.4 \times 10^{33}\ \text{years} \cdot \left(\frac{\Lambda_{\mathrm{GUT}}}{10^{15}\ \mathrm{GeV}}\right)^4 \cdot \frac{1}{|\tilde{c}_I|^2}. \tag{3}$$

Prior to lattice QCD, matrix elements of these effective operators were estimated using the nonrelativistic quark model of the nucleon [30], the chiral lagrangian [31], and the MIT bag model [32,33]. Eliminating model uncertainty requires *ab initio* QCD calculations on a lattice, which have been pursued with improving methodology since nucleon structure calculations became possible. Amplitudes of transitions from a nucleon to a meson state can be approximated using proton-to-vacuum (annihilation) decay constants determined on a lattice and Chiral perturbation theory (ChPT) [34] (the so-called "indirect method"). Alternatively, these amplitudes can be computed on a lattice directly, which enables better control of systematic effects. The former method was used quenched-QCD calculations with Wilson valence quark action [35–37] and domain wall fermion (DWF) action [38], as well as in unitary QCD with dynamical DWF action [39]. Direct calculation of proton-to-meson transition matrix elements was performed in quenched QCD with Wilson valence quarks [40] and DWF quarks [38], as well as in unitary QCD with $N_f = 2+1$ dynamical domain wall fermions [41,42]. In Refs. [38,40,42], results from the indirect method were also reported.

Although significant progress has been made in improving calculations of proton decay amplitudes, some important systematic uncertainties are still remaining. The most recent direct calculation [42] reports uncertainty 20%–40% in the proton decay amplitudes, and also reports disagreement between the direct and the indirect methods. Since the indirect method relies on ChPT, it is plausible that the pion masses $m_\pi \gtrsim 340$ MeV used in that calculation were too heavy for the ChPT to work. However, direct-method transition amplitudes computed with unphysical heavy pion masses also require chiral extrapolation, which may also result in systematic uncertainty. In particular, in the framework of the chiral-bag proton model, it has been suggested that the proton-decay matrix elements may depend dramatically on the quark mass [33]. If this is the case, some GUT models [e.g., SUSY- and regular $SU(5)$] may evade constraints even with the presently available experimental data. It is also important to note that the effective proton decay operators (1) contain chiral quark fields, and preserving chiral symmetry is particularly challenging in lattice calculations. Some of the (valence) quark actions used in earlier calculations [35–37,40] break chiral symmetry explicitly.

In this work, we study proton decay matrix elements using chirally symmetric dynamical $N_f = 2+1$ and valence domain wall fermions with physical quark masses. We compute these matrix elements with both the direct and indirect methods and compare their results. A formidable progress has been made towards lattice calculations with chiral fermions at the physical point [43–45]. We use two ensembles with lattice spacings $a = 0.20$ fm and $a = 0.14$ fm and explore different kinematics in order to obtain reliable interpolation to the physical decay kinematic points. Together with nonperturbative renormalization and analysis of nucleon and meson excited states, our calculation aims to eliminate common lattice QCD systematic effects.

---

[2] Throughout the paper, we use Euclidean conventions for γ-matrices (see, e.g., Ref. [29]), so that $C = \gamma_2\gamma_4$.

Another potential proton decay channel is into three leptons or a lepton and one or more photons [46–48]. Such processes can occur either through effective dimension-nine operators [47], which may only be relevant if the BSM physics scale $\Lambda_{\rm BSM} \ll \Lambda_{\rm GUT}$, or through emission of a photon from quark or charged lepton involved into effective dimension-six interaction (1). Decays into three leptons have also been constrained with data from Super Kamiokande; for example, $\tau/{\rm Br}(p \to \ell\bar{\ell}'\bar{\ell}'') \geq (0.9\ldots3.4)\times 10^{34}$ years for $\ell = e\mu$ [49]. Rates of such processes depend on the same proton decay constants $\langle{\rm vac}|\mathcal{O}_I|p\rangle$ as the ones in the indirect calculation of proton decay amplitudes $p \to \Pi\ell$ mentioned above. We report results of nonperturbative lattice calculations of both proton-meson and proton-vacuum amplitudes that are important to proton decay phenomenology.

Another baryon-number violating process that could be responsible for baryogenesis is the six-quark interaction leading to nonconservation of the $(B-L)$ number and $|\Delta B| = 2$ transitions. Such events are potentially observable as neutron-antineutron oscillations [50], and their matrix elements have been recently computed on a lattice with chirally symmetric action at the physical point [29,51].

The paper is organized as follows. In Sec. II, we introduce our conventions and notations, and describe our methodology and lattice QCD setup for computing nucleon-meson matrix elements. A detailed discussion of nonperturbative renormalization methodology and results is presented in Sec. III. In Sec. IV, we show details of our analysis and present our results for proton and meson spectra, proton decay amplitudes, and proton decay constants obtained on the two lattice QCD ensembles as well as in the continuum limit. Finally, in Sec. V we compare our results to previous calculations, discuss systematic errors in our calculation, discuss the impact of our results, and suggest further directions to improve systematic uncertainties.

II. METHODOLOGY

A. Operator definitions

The minimal complete set of the lowest-dimension effective proton decay operators symmetric under $SU(3)_c \times SU(2)_{\rm EW} \times U(1)$ has been constructed in Refs. [27,28,52]. Using notation of Refs. [40,52], these operators are

$$\mathcal{O}^{(1)}_{abcd} = (\bar{D}^C_{ia} U_{jb})_R (\bar{Q}^C_{\alpha kc} L_{\beta d})_L \epsilon_{ijk}\epsilon_{\alpha\beta}, \tag{4}$$

$$\mathcal{O}^{(2)}_{abcd} = (\bar{Q}^C_{\alpha ia} Q_{\beta jb})_L (\bar{U}^C_{kc} l_d)_R \epsilon_{ijk}\epsilon_{\alpha\beta}, \tag{5}$$

$$\bar{\mathcal{O}}^{(4)}_{abcd} = (\bar{Q}^C_{\alpha ia} Q_{\beta jb})_L (\bar{Q}^C_{\gamma kc} L_{\delta d})_L \epsilon_{ijk}\epsilon_{\alpha\delta}\epsilon_{\beta\gamma}, \tag{6}$$

$$\mathcal{O}^{(5)}_{abcd} = (\bar{D}^C_{ia} U_{jb})_R (\bar{U}^C_{kc} l_d)_R \epsilon_{ijk}, \tag{7}$$

where a, b, c, d are generation indices, i, j, k are $SU(3)_c$ indices, α, β, γ, δ are the indices of the left-handed $SU(2)_{\rm EW}$ fermion doublets, and 2-spinors of the indicated chirality (R, L) are contracted inside the parentheses. From now on, we will omit the color indices and imply contraction with the antisymmetric tensor ϵ_{ijk}. These operators conserve the $(B-L)$ number, and the outgoing antilepton (e^+, μ^+, $\bar{\nu}$) may have only electroweak interaction with quark fields present in the initial and final states, which may be neglected at the hadronic scale. The amplitude $p \to \Pi\ell$ may then be factorized into

$$\mathcal{M}(p \to \Pi\ell) = \bar{v}^C_{\ell\alpha}(\vec{q})\langle\Pi(\vec{p}')|(\bar{q}_1{}^C q_2)_\chi q_{3\chi'\alpha}|N(\vec{k})\rangle, \tag{8}$$

where $\chi^{(\prime)} = R, L$ denotes chirality and $\bar{v}^C_\ell$ is the spinor of the antilepton in the final state with momentum $\vec{q} = \vec{k} - \vec{p}$. To avoid redundancy due to parity symmetry, we will only consider combinations $(\chi, \chi') = (L, L)$ and (R, L) below. The following quark combinations $q_{1,2,3}$ are possible for the initial proton $N = p$ and the energy-allowed final meson $\Pi = \pi^0$, π^+, K^0, K^+, and η states,

$$\begin{aligned} &\langle\pi^0|(\bar{u}^C d)_\chi u_L)|p\rangle, \\ &\langle\pi^+|(\bar{u}^C d)_\chi d_L)|p\rangle = U_{1\chi}, \\ &\langle K^0|(\bar{u}^C s)_\chi u_L)|p\rangle = S_{1\chi}, \\ &\langle K^+|(\bar{u}^C s)_\chi d_L)|p\rangle = S_{2\chi}, \\ &\langle K^+|(\bar{u}^C d)_\chi s_L)|p\rangle = S_{3\chi}, \\ &\langle K^+|(\bar{d}^C s)_\chi u_L)|p\rangle = S_{4\chi}, \\ &\langle\eta|(\bar{u}^C d)_\chi u_L)|p\rangle = S_{5\chi}. \end{aligned} \tag{9}$$

Similar quark combinations can be enumerated for neutron decays, and their relation to the proton matrix elements under isospin symmetry can be found in Ref. [41]. In addition, isospin symmetry requires that

$$\langle\pi^0|(\bar{u}^C d)_\chi u_L|p\rangle = \frac{1}{\sqrt{2}}\langle\pi^+|(\bar{u}^C d)_\chi d_L|p\rangle = \frac{1}{\sqrt{2}} U_{1\chi}, \tag{10}$$

which is precisely fulfilled in our $SU(2)_f$-symmetric calculation at the contraction level. Computing amplitudes of η-channel decays ($S_{5\chi}$) require disconnected quark contractions. Such calculation is challenging with DW fermions at the physical point, and we omit these amplitudes in the present work.

Matrix elements between the proton and the meson + lepton pair in Eq. (8) may be decomposed into linear combinations of two form factors $W_{0,1}$ [40],[3]

---

[3] The conventions for on-shell nucleon u_N and antilepton $\bar{v}^C_\ell$ states can be found in Appendix A.

$$\begin{aligned}
&\bar{v}^C_{\ell\alpha}(\vec{q})\langle\Pi(\vec{p})|\mathcal{O}^{\chi\chi'}_\alpha(q)|N(\vec{k})\rangle \\
&\quad= \left(\bar{v}^C_\ell(\vec{q})P_{\chi'}\left[W^{\mathcal{O}}_0(Q^2) - \frac{i\not{q}}{m_N}W^{\mathcal{O}}_1(Q^2)\right]u_N(\vec{k})\right) \\
&\quad\approx [\bar{v}^C_\ell(\vec{q})P_{\chi'}u_N(\vec{k})]W_0(-m^2_\ell) + O(m_\ell/m_N), \qquad (11)
\end{aligned}$$

where $Q^2 = -q^2 = -(E_N - E_\Pi)^2 + (\vec{k} - \vec{p})^2$ and $\bar{v}^C_\ell(\vec{q})$ is the spinor of the antilepton in the final state. In the last line, the contribution of the form factor W_1 can be neglected in decays into positrons and antineutrinos but not for antimuons with $m_\ell/m_N \approx 0.1$. Also, unless the outgoing antilepton is ultrarelativistic, there is interference between left- and right-handed amplitudes, and the decay rate (2) takes the form

$$\Gamma(p \to \Pi\bar{\ell}) = \frac{1}{8\pi}\frac{E_\ell|\vec{q}_\ell|}{m_N}\left(\mathcal{A} - \frac{m_\ell}{E_\ell}\mathcal{B}\right), \qquad (12)$$

where E_ℓ and $\vec{q}_\ell$ are the outgoing antilepton energy and momentum, and

$$\mathcal{A} = |W^L_{\bar{\ell}}|^2 + |W^R_{\bar{\ell}}|^2, \qquad (13)$$

$$\mathcal{B} = 2\mathrm{Re}[W^L_{\bar{\ell}}(W^R_{\bar{\ell}})^*], \qquad (14)$$

and the on-shell antilepton helicity matrix elements are[4]

$$\begin{aligned}
W^L_{\bar{\ell}} &= \sum_{i,\chi}\left[C^{i,\chi L}W^{i,\chi L}_0 - \frac{m_\ell}{m_N}C^{i,\chi R}W^{i,\chi R}_1\right]_{Q^2=-m^2_\ell}, \\
W^R_{\bar{\ell}} &= \sum_{i,\chi}\left[C^{i,\chi R}W^{i,\chi R}_0 - \frac{m_\ell}{m_N}C^{i,\chi L}W^{i,\chi L}_1\right]_{Q^2=-m^2_\ell}, \qquad (15)
\end{aligned}$$

[the summation over i does not include the χ, χ' helicities (8), unlike I in Eqs. (1) and (2)]. In the $m_\ell \to 0$ limit, the interference contribution $\mathcal{B}$ disappears, and the decay rate (12) is simplified to Eq. (2).

For indirect evaluation of the $p \to \Pi\bar{\ell}$ amplitudes using chiral perturbation theory, as well as computing 3ℓ- or $\ell\gamma$-channel decay amplitudes, one needs the nucleon decay constants from the following matrix elements

$$\begin{aligned}
\langle\mathrm{vac}|(\bar{u}^C d)_R u_L|N\rangle &= \alpha P_L u_N, \\
\langle\mathrm{vac}|(\bar{u}^C d)_L u_R|N\rangle &= -\alpha P_R u_N, \\
\langle\mathrm{vac}|(\bar{u}^C d)_L u_L|N\rangle &= \beta P_L u_N, \\
\langle\mathrm{vac}|(\bar{u}^C d)_R u_R|N\rangle &= -\beta P_L u_N. \qquad (16)
\end{aligned}$$

Combinations of these constants

$$\langle\mathrm{vac}|(\bar{u}^C\gamma_5 d)u|N\rangle = (\alpha - \beta)u_N, \qquad (17)$$

$$\langle\mathrm{vac}|(\bar{u}^C d)\gamma_5 u|N\rangle = -(\alpha + \beta)u_N, \qquad (18)$$

yield the overlap of the positive-parity nucleon ground state with nonrelativistic (scalar diquark and upper u-quark) and relativistic (pseudoscalar diquark and lower u-quark) nucleon interpolating fields, respectively. In the nonrelativistic limit corresponding to calculations with unphysical heavy u, d quark masses, it is expected that $|\alpha + \beta| \ll |\alpha - \beta|$. In the "indirect" method, proton decay amplitudes are combinations of the low-energy constants α, β, quark contributions to the baryon spin, and the meson decay constants $f_{\pi,K}$ [40,42]. These formulas are collected in Appendix B for completeness.

B. Lattice setup

For our calculation, we use physical-point ensembles of gauge fields on $24^3 \times 64$ [43] and $32^3 \times 64$ [53] lattices ensembles with spatial volumes $\approx(4.8\ \mathrm{fm})^3$ and $(4.6\ \mathrm{fm})^3$, respectively. These ensembles have been generated by the RBC/UKQCD collaboration using I-DSDR gauge action and $N_f = 2 + 1$ flavors of dynamical quarks with Möbius domain wall fermion (MDWF) action. These MDWF fermions possess chiral symmetry due to the additional fifth dimension of $L_5 = 24$ and $L_5 = 12$, respectively, which are sufficient to suppress chiral symmetry breaking effects otherwise present in lattice fermion actions. To soften explicit chiral symmetry breaking effects due to the relatively large lattice spacing, these ensembles also employ the dislocation-suppressing-determinant-ratio (DSDR) [54]. Lattice spacings, bare quark masses, pseudoscalar meson masses, and other parameters are summarized in Table I. The masses of mesons and of the proton are reported below in Sec. IV A. As our lattices are nearly precisely at the physical point, our results below will not require chiral extrapolation. Slight deviations of the pion and kaon masses from their physical values can be, in principle, rectified by ChPT-inspired corrections to our results, but the precision we aim for in this work does not warrant such a step.

In order to make the numerical calculation affordable, we perform *"all-mode-averaging" (AMA)* sampling [57], in which we approximate the light and strange quark propagators with truncated solutions to the MDWF operator [58]. On the 24ID ensemble, the MDWF operator itself is approximated with "z-Möbius" operator, in which complex coefficients b_5, c_5 are varied along the fifth dimension so that it can be reduced to $L_{5s} = 12$ while keeping the residual mass m_{res} the same. For a better approximation of the low-eigenmode space of the light-quark Dirac operator, we augment the truncated conjugate-gradient (CG) solver with deflation using a combination of exact and coarse-blocked eigenvectors, which are computed with multigrid Lanczos algorithm [59]. On each gauge configuration, we

---

[4] The $O(W_1)$ correction to the two-body decay amplitude given in Ref. [42] is oversimplified and confusing. The correct formulas are given here.

TABLE I. Lattice parameters for the 24ID and 32ID ensembles. Both ensembles have I-DSDR gauge and (zMöbius) domain wall fermion actions. The pion and kaon masses are determined in our analysis (see Sec. IV A). Lattice spacings and residual masses are computed elsewhere [45,55,56]. In the last group of columns, we show the number of light-quark deflation eigenvectors, the numbers of conjugate gradient (CG) iterations to compute light-quark and strange-quark propagators for approximate samples, and the number of gauge configurations analyzed.

$L_x^3 \times L_t$	a^{-1}[GeV]	β	$L_{5f}(L_{5s})$	M_5	am_{res}	am_l	am_s	am_π	am_K	$m_\pi L$	$N_{\text{EV}}(N_{\text{basis}})$	$N_{\text{CG}}^{u/d}$	N_{CG}^s	N_{cfg}
$24^3 \times 64$	1.023(2)	1.633	32/12	1.8	0.00228(1)	0.00107	0.0850	0.1378(7)	0.5004(25)	3.31	2000(1000)	300	200	140
$32^3 \times 64$	1.378(5)	1.75	12/12	1.8	0.00189(1)	0.0001	0.0450	0.1008(5)	0.3543(6)	3.25	2000(250)	200	200	112

compute 32 approximate ("sloppy") samples with such truncated quark propagators. In order to correct for any potential bias, we recompute one sample on each configuration using exact quark propagators. We find that with our parameters the AMA approximation is very efficient, i.e., the statistical variance of the difference between the approximate and exact samples is negligible, and the statistical precision is always dominated by fluctuations in the approximate samples.

C. Nucleon-meson correlators on a lattice

In order to compute the matrix elements in Eqs. (11) and (16) on a lattice, we evaluate three-point correlation functions of proton creation $\bar{N}$, proton decay $\mathcal{O}_\alpha^\chi = (\bar{q}_1^C q_2)_\chi q_{3L\alpha}$, and meson annihilation J_Π operators,

$$C_{\alpha\beta}^{\Pi\mathcal{O}N}(\vec{p},\vec{q};t_2,t_1) = \sum_{\vec{y},\vec{z}} e^{-i\vec{p}\,\vec{y}-i\vec{q}\,\vec{z}+i\vec{k}\,\vec{x}} \cdot \langle J_\Pi(\vec{y},x_4+t_2)\mathcal{O}_\alpha^{\chi\chi'}(\vec{z},x_4+t_1)\bar{N}_\beta(x)\rangle. \tag{19}$$

The spin indices are contracted with polarization matrices $\mathcal{P}$

$$C_{\mathcal{P}}^{\Pi\mathcal{O}N} = \mathcal{P}_{\beta\alpha} C_{\alpha\beta}^{\Pi\mathcal{O}N}, \tag{20}$$

that yield nontrivial combinations of proton decay form factors $W_{0,1}$ The nucleon and meson interpolating operators are

$$N = \epsilon^{ijk}(\tilde{u}^{iT} C\gamma_5 \tilde{d}^j)\tilde{u}^k, \tag{21}$$

$$J_{\pi^+} = \bar{\tilde{d}}\gamma_5\tilde{u}, \tag{22}$$

$$J_{\pi^0} = \frac{1}{\sqrt{2}}(\bar{\tilde{u}}\gamma_5\tilde{u} - \bar{\tilde{d}}\gamma_5\tilde{d}), \tag{23}$$

$$J_{K^+} = \bar{\tilde{s}}\gamma_5\tilde{u}, \tag{24}$$

$$J_{K^0} = \bar{\tilde{s}}\gamma_5\tilde{d}, \tag{25}$$

$$J_\eta = \frac{1}{\sqrt{6}}(\bar{\tilde{u}}\gamma_5\tilde{u} + \bar{\tilde{d}}\gamma_5\tilde{d} - 2\bar{\tilde{s}}\gamma_5\tilde{s}), \tag{26}$$

where the component quark fields $\tilde{u}, \tilde{d}, \tilde{s}$ are smeared with gauge-invariant Wuppertal smearing [60] using APE-smeared gauge links. The smearing parameters are collected in Table II.

In the case of π and K mesons in the final states, contractions of quark fields in the operators (19) generate only connected diagrams, while in the case of the η meson, there are combinations of both connected and disconnected diagrams. At the physical point, contributions from disconnected diagrams in the η correlators can be large; since we do not evaluate disconnected contractions in this work, decays in the η-channel are not studied here. We use the standard sequential propagator technique to compute connected contributions to the three-point function (19). First, we compute a forward quark propagator from a smeared source located at the origin of a particular sample x on the time slice $t_0 = x_4$. Then, we compute a backward propagator from a sequential source that is constructed with one of the momentum-projected meson interpolation operators $e^{-i\vec{p}\,\vec{y}}(\bar{\tilde{q}}_2\Gamma\tilde{q}_1)_{\vec{y}}$ restricted to the "sink" time slice $t_0 + t_2$. Finally, the backward propagator is contracted with the two forward propagators at the operator insertion point, and the result is projected on momentum $\vec{q}$.

With two momentum projections in Eq. (19), the initial nucleon momentum $\vec{k} = \vec{p} + \vec{q}$ is determined by the momentum conservation after averaging over a gauge ensemble. We select kinematic points $(\vec{p},\vec{q})$ so that 1. the lepton is close to being on-shell, $|q^2| = |(k-p)^2| \lesssim m_\ell^2$, 2. the nucleon spatial momentum is small to minimize statistical fluctuations, and 3. the decay kinematic point $q^2 \approx 0$ is bracketed enabling a reliable *interpolation*. The selected initial and final state momenta combinations are shown in Table III. Since the physical volumes on both lattice ensembles are very close, so are the quanta $2\pi/(aL)$ of spatial momentum, which result in identical selections of

TABLE II. Parameters for covariant Gaussian smearing of quark sources and APE smearing of the gauge fields used in their construction.

	A_{APE}	N_{APE}	α_{Wup}	N_{Wup}
24ID	2.85	25	2.5	10
32ID	2.85	25	2.5	40

TABLE III. Initial and final momenta in the three-point functions selected for close-to-physical kinematics $|q^2| \lesssim m_\ell^2$ using masses determined from fits on a lattice (see Sec. IV A).

			$Q^2(\mathrm{GeV}^2)$	
Π	$\vec{n}_\Pi$	$\vec{n}_N$	(24ID)	(32ID)
π	[1 1 1]	[0 0 0]	−0.011	0.020
	[1 1 1]	[0 1 0]	−0.117	−0.089
	[0 0 2]	[0 0 0]	0.120	0.150
K	[0 1 1]	[0 0 0]	0.038	0.047
	[0 1 1]	[0 1 0]	−0.057	−0.052
	[0 0 1]	[0 0 0]	−0.074	−0.070

lattice momenta and only slightly different q^2 values for the two ensembles. In order to further reduce the cost of our computation, we use the "coherent trick", in which backward propagators for two maximally separated samples are computed simultaneously from the sum of their respective sequential sources.

Meson and nucleon two-point functions,

$$C^{\Pi\Pi}(\vec{k},t) = \sum_{\vec{x}} e^{-i\vec{p}\,\vec{x}} \langle J_\Pi(x) J_\Pi^\dagger(0)\rangle, \tag{27}$$

$$C_+^{N\bar{N}} = \mathrm{Tr}\left[\frac{1+\gamma_4}{2} C^{N\bar{N}}\right],$$

$$C_{\alpha\beta}^{N\bar{N}}(\vec{k},t) = \sum_{\vec{x}} e^{-i\vec{k}\,\vec{x}} \langle N_\alpha(x) \bar{N}_\beta(0)\rangle, \tag{28}$$

are also evaluated to compute their energies as well as overlaps of their interpolating operators (21)–(26) with their respective ground states. Similarly to the three-point functions, only the correlators with η mesons require disconnected diagrams, which are not studied in the present work. For the nucleon, we use the positive-parity projected spinor for all momenta $\vec{k}$. Although with $\vec{k} \neq 0$ the nucleon does not have definite parity, our momenta are small enough for it to be a good approximation for the ground-state nucleon.

D. Proton decay matrix elements

In the large-time limit $\{t_1, (t_2 - t_1)\} \to \infty$, the three-point correlation functions (20) are dominated by the ground-state proton-meson amplitude. However, in our lattice calculation the time separations may be not large enough to neglect contributions from their excited states. The spectral decomposition of a three-point correlation function yields

$$\begin{aligned} C_{\alpha\beta}^{\Pi\mathcal{O}\bar{N}}(\vec{p},\vec{q};t_2,t_1) = \sum_{m,n,s} \langle\Omega|J_\Pi|\Pi_m(\vec{p})\rangle \frac{e^{-E_{\Pi,m}(t_2-t_1)}}{2E_{\Pi,m}} \cdot \\ \cdot \langle\Pi_m(\vec{p})|\mathcal{O}_\alpha|N_n^{(s)}(\vec{k})\rangle \frac{e^{-E_{N,n}t_1}}{2E_{N,n}} \\ \times \langle N_n^{(s)}(\vec{k})|\bar{N}_\beta|\Omega\rangle, \end{aligned} \tag{29}$$

where indices m, n denote the ground $(m, n = 0)$ and excited meson $(m > 0)$ and nucleon $(n > 0)$ states. The ground state matrix elements $M_{\alpha,s}^{00}(q) = \langle\Pi_0(\vec{p})|\mathcal{O}_\alpha|N_0^{(s)}(\vec{k})\rangle$ dominate this sum for $\{t_1, (t_2 - t_1)\} \to \infty$. Lattice interpolating fields for the meson J_Π and the nucleon N may have arbitrary normalizations due to quark smearing, which are reflected in their *overlap* factors Z_Π and Z_N,

$$\langle\Omega|J_\Pi|\Pi_0(\vec{p})\rangle = \sqrt{Z_\Pi(\vec{p})}, \tag{30}$$

$$\langle N_0^{(s)}(\vec{k})|\bar{N}_\alpha|\Omega\rangle = \bar{u}_\alpha^{(s)} \sqrt{Z_N(\vec{k})}. \tag{31}$$

These momentum-dependent factors may obtained from ground-state terms in their respective two-point correlation functions,

$$C^{\Pi\Pi}(\vec{p},t)|_{\mathrm{g.s.}} = \frac{Z_\Pi(\vec{p})}{2E_\Pi} e^{-E_\Pi t}, \tag{32}$$

$$\begin{aligned} C_+^{N\bar{N}}(\vec{k},t)|_{\mathrm{g.s.}} &= \frac{Z_N(\vec{k})}{2E_N} \mathrm{Tr}[\mathcal{P}_+(-i\not{k} + m_N)] e^{-E_N t} \\ &= Z_N(\vec{k}) \frac{E_N + m_N}{E_N} e^{-E_N t}. \end{aligned} \tag{33}$$

We perform two-state fits to $C^{\Pi\Pi}(t)$ and $C_+ = \mathrm{Tr}[\mathcal{P}_+ C^{N\bar{N}|}(t)$

$$C^{\Pi\Pi}(\vec{p};t) = C_{\Pi,0} e^{-E_{\Pi,0}t} + C_{\Pi,1} e^{-E_{\Pi,1}t}, \tag{34}$$

$$C_+^{N\bar{N}}(\vec{k};t) = C_{N,0} e^{-E_{N,0}t} + C_{N,1} e^{-E_{N,1}t}, \tag{35}$$

independently for each momentum $\vec{p}$, $\vec{k}$ and extract the ground-state overlap factors for the meson and the nucleon

$$Z_\Pi(\vec{p}) = 2E_{\Pi,0} C_{\Pi,0}, \qquad Z_N(\vec{k}) = \frac{E_{N,0}}{E_{N,0} + m_N} C_{N,0}. \tag{36}$$

In order to compute the form factors (11), we project the three-point function $\mathrm{Tr}[\mathcal{P} C^{\Pi\mathcal{O}\bar{N}}] = C_\mathcal{P}^{\Pi\mathcal{O}\bar{N}}$ with a set of suitable projectors

$$\{\mathcal{P}\} = \{P_+, P_+\gamma_j\}, \quad \text{where } j = 1,2,3, \quad P_+ = \frac{1+\gamma_4}{2}. \tag{37}$$

Similarly to the meson and nucleon two-point functions (32), (33), the ground-state contribution to a spin-projected three-point function (20) can be written as

$$\begin{aligned} C_\mathcal{P}^{\Pi\mathcal{O}\bar{N}}(\vec{p},\vec{q};t_2,t_1)|_{\mathrm{g.s.}} \\ = \frac{\sqrt{Z_\Pi Z_N}}{4E_\Pi E_N} e^{-E_\Pi(t_2-t_1) - E_N t_1} \cdot \\ \cdot \mathrm{Tr}\left[\mathcal{P}\mathcal{P}_\chi \left(W_0^\mathcal{O} - \frac{i\not{q}}{m_N} W_1^\mathcal{O}\right)(-i\not{k} + m_N)\right], \end{aligned} \tag{38}$$

where the matrix element $M^{00}_{\alpha,s}(q)$ is decomposed into decay form factors $W_{0,1}$. However, before these form factors can be extracted, the ground-state matrix element $M^{00}_{\alpha,s}(q)$ must be isolated from excited-state contamination. For this purpose, we study the time dependence of the projected three-point function (38) with two methods described below.

The *plateau method* is based on a ratio of correlation functions

$$R^{\mathcal{O}}_{\mathcal{P}}(\vec{p},\vec{q};t_2,t_1) = \frac{\sqrt{Z_\Pi(\vec{p})Z_N(\vec{k})}C^{\Pi\mathcal{O}\bar{N}}_{\mathcal{P}}(\vec{p},\vec{q};t_2,t_1)}{C^{\Pi\Pi}(\vec{p},t_2-t_1)C^{N\bar{N}}_{+}(\vec{k},t_1)}, \quad (39)$$

where the $Z_{\Pi,N}$ overlap factors (36) are extracted from the fits to the two-point functions (34), (35). The values of this ratio near the center of the plateau, $t_1 \approx t_2/2$, must converge to the ground-state matrix element for large time separation t_2. Deviations from the ground state are suppressed as $\mathcal{O}(e^{-\Delta E_\Pi(t_2-t_1)}, e^{-\Delta E_N t_1})$, and the plateaus are expected to converge to ground-state values faster for $t_1 > t_2/2$, i.e., closer to the meson sink rather than the proton source because of the larger energy gap of the former. However, the noise is also expected to be larger in this region due to the much larger nucleon mass. For each value of t_2, we calculate the average of two or three central plateau points $\bar{R}(t_2)$ and estimate statistical errors using bootstrap. Convergence of the $\bar{R}(t_2)$ values with increasing t_2 indicates suppression of excited states and allows us to estimate related systematic effects.

The *two-state fit method* is intended to take into account the excited states in a systematic fashion and reduce the bias associated with them. Similarly to the two-point function fits [see (34)and (35)], we include single excited states for both the meson and the proton, and perform correlated least-χ^2 fits

$$C^{\Pi\mathcal{O}\bar{N}}_{\mathcal{P}}(\vec{p},\vec{q};t_2,t_1) = \sum_{m,n=0,1} C^{\Pi\mathcal{O}\bar{N}}_{\mathcal{P},mn} e^{-E_{\Pi,m}(t_2-t_1)-E_{N,n}t_1}. \quad (40)$$

Discarding the excited state contributions, we define the equivalent of the ratio (39) that contains only the ground-state contributions

$$R^{\Pi\mathcal{O}\bar{N}}_{\mathcal{P},00}(\vec{p},\vec{q}) = \frac{\sqrt{Z_\Pi(\vec{p})Z_N(\vec{k})}C^{\Pi\mathcal{O}\bar{N}}_{\mathcal{P},00}}{C_{\Pi,0}C_{N,0}}, \quad (41)$$

and must be equal to the converged value of Eq. (39) at $\{t_1,(t_2-t_1)\} \to \infty$. Systematic uncertainties in this method are estimated by comparing fit results performed in ranges $t^N_{\mathrm{skip}} \le t_1 < (t_2 - t^\Pi_{\mathrm{skip}})$ with varying $t^{N,\Pi}_{\mathrm{skip}}$. $t_{\mathrm{skip}} = 2$ and $t_{\mathrm{skip}} = 3$, all of which yielded reasonable χ^2 values.

These methods are applied independently to each combination of initial and final momenta in Table III and for all nontrivial spin projections $\mathcal{P}$ of the tree-point correlation functions.

E. Proton decay form factors

While only the W_0 form factor is necessary for computing width of decays into e^+ and $\bar{\nu}$, the W_1 form factor is also necessary for decays into μ^+. In order to disentangle form factors $W_{0,1}$, one needs at least two independent matrix elements $M^{00}_{\alpha,s}(q)$ in Eq. (29) or, equivalently, two independent nontrivial projections of the three-point functions (38). Evaluating the spin traces in Eq. (38) leads to the following (ground-state) contributions to the ratios [(39) and (41)]

$$R^{\Pi\mathcal{O}\bar{N}}_{P_+} = \frac{1}{2}W_0 + \left(\frac{\Delta E}{2m_N} - \frac{\vec{k}\cdot\vec{q}}{2m_N(E_N+m_N)}\right)W_1, \quad (42)$$

$$R^{\Pi\mathcal{O}\bar{N}}_{P_+\gamma_i} = \frac{-ik_i}{2(E_N+m_N)}W_0 + \frac{-i(E_N+m_N)q_i + i\Delta E k_i \pm (\vec{q}\times\vec{k})_i}{2m_N(E_N+m_N)}W_1, \quad (43)$$

where $\Delta E = E_N - E_\pi$ and the ($\pm$) sign corresponds to the decay operator helicity $\chi' = R,\ L$, respectively. These equations take into account nonzero nucleon momentum $\vec{k}$, which is useful for a better approximation of the physical kinematic point $q^2 \approx 0$. All previous proton decay calculations were done with zero nucleon momentum $\vec{k} = 0$ [41].

We take a projection of Eq. (43) on the spatial vector $\vec{q}$ in order to simplify computing the form factors and obtain

$$R_{P_+(i\vec{q}\cdot\vec{\gamma})} = \sum_i i\vec{q}_i R_{P_+\gamma_i} = \frac{\vec{k}\cdot\vec{q}}{2(E_N+m_N)}W_0 + \left(\frac{\vec{q}^2}{2m_N} - \frac{\Delta E(\vec{k}\cdot\vec{q})}{2m_N(E_N+m_N)}\right)W_1. \quad (44)$$

While it is possible to perform "overdetermined" fits by considering $P_+\gamma_i$ polarization projections separately, doing so would accomplish only a check of the rotational symmetry.

III. RENORMALIZATION

A. Nonperturbative renormalization scheme

The bare hadronic matrix elements computed on a lattice have to be converted to a continuum renormalization scheme such as $\overline{\mathrm{MS}}$ that is used in proton decay phenomenology. Operators are defined on a lattice at a relatively low scale of $a^{-1} \approx$ 1–2 GeV, where the strong coupling α_S is large. Nonperturbative renormalization avoids major systematic effects due to truncation of perturbative series on a lattice and is required to achieve reliable and precise results. In a typical approach called Rome-Southampton method [61], one computes correlators of a bare operator with bare *external* quark and gluon fields carrying large virtual momenta in a fixed gauge and compares their behavior to a perturbative prediction, resulting in a finite conversion factor from lattice to a perturbative renormalization scheme, e.g., to $\overline{\rm MS}$. The Landau gauge is typically employed as straightforward to implement consistently between lattice and continuum.

Such an intermediate scheme requires an additional perturbative conversion to the $\overline{\rm MS}$ scheme; in addition, lattice field correlators may have nonperturbative infrared contributions. Systematic effects from both of these sources depend on the configuration of external field momenta. In the case of some quark-bilinear operators, selecting a *nonexceptional* momentum configuration ("SMOM" scheme) is crucial for avoiding large nonperturbative effects that may appear if the operator carries zero momentum ("MOM" scheme) [62]. In the case of the three-quark operators, momenta can be arranged in even more ways. The two choices discussed in the literature are either with all three quarks carrying the same momentum p [38] or carrying momenta of the same magnitude $p^2 = k^2 = r^2$ that add to zero vertex momentum $p + k + r = 0$ [63]; below we will refer to these momentum arrangements as "MOM3q" and "SYM3q", respectively, to discriminate from the schemes used for quark-bilinear operators.

In order to avoid both discretization and nonperturbative effects, the momenta of the fields must satisfy the "scale window" condition

$$\Lambda_{\rm QCD} \ll p \ll (\pi/a). \tag{45}$$

The three-quark operator in the correlator following the MOM3q scheme will carry momentum $(3p)^2$ and may require a wider scale window, which is challenging on coarse lattice ensembles that are used in the present work. Additionally, the large vertex momentum may result in large perturbative conversion factors to the $\overline{\rm MS}$ scheme and, consequently, larger systematic uncertainties. Indeed, the amputated Green's function of the three-quark operator at the $O(\alpha_S)$ order is larger[5] in the MOM3q scheme [38,64] compared to the SYM3q scheme [63,65] (see also Appendix C)

$$[\Lambda_{3q}^{\overline{MS}}]_{\rm MOM3q} \approx 1 + (-4.060)\frac{\alpha_s}{4\pi} + O(\alpha_S^2), \tag{46}$$

$$[\Lambda_{3q}^{\overline{MS}}]_{\rm SYM3q} \approx 1 + (0.989)\frac{\alpha_s}{4\pi} + O(\alpha_S^2). \tag{47}$$

The SYM3q Green's function (47) is available up to $O(\alpha_S^2)$ order [63], while the MOM3q Green's function (46) is available only up to $O(\alpha_S)$ [38,64]. The large difference at the $O(\alpha_S)$ order indicates that the unknown $O(\alpha_S^2)$ correction to the former may also be larger compared to the latter, which has been computed and can be used for more accurate perturbative matching. On the other hand, in the SYM3q scheme, the vertex carries zero momentum $q = p + k + r = 0$, which might result in a nonperturbative contribution from the nucleon pole $\sim(q^2 + m_N^2)^{-1}$. However, the overlap of a point-localized three-quark operator with the nucleon state is suppressed due to the nonzero nucleon size. Since most of the nucleon mass comes from the glue (as shown by the momentum sum-rule in deep inelastic scattering experiments [66]) and the nucleon remains massive in the chiral limit, such a pole contribution should be negligible. Therefore, we select the SYM3q scheme because it enables better control of these systematic uncertainties.

B. Renormalization of decay operators

In order to determine nonperturbative renormalization factors, we compute Green's functions of operators (9) with three external quark fields carrying definite Euclidean 4-momenta. There are two flavor structures

$$[\mathcal{O}^{(ud)s}_{\Gamma\Gamma'}]_\delta = \epsilon^{abc}(\bar{u}^{Ta}\Gamma d^b)\Gamma' s^c_\delta, \tag{48}$$

$$[\mathcal{O}^{(ud)d}_{\Gamma\Gamma'}]_\delta = \epsilon^{abc}(\bar{u}^{Ta}\Gamma d^b)\Gamma' d^c_\delta, \tag{49}$$

with ten linearly-independent Lorentz-invariant choices of $(\Gamma\otimes\Gamma') = \{SS, PP, AA, VV, TT, SP, PS, AV, VA, TQ\}$,[6] of which five are positive parity and five are negative parity. The labels S, P, V, A, T, Q stand for $\Gamma^{(\prime)} = 1, \gamma_5, \gamma_\mu, \gamma_\mu\gamma_5, \sigma_{\mu\nu}, \sigma_{\mu\nu}\gamma_5$, respectively, with Lorentz indices μ, ν contracted in $(\Gamma\otimes\Gamma')$.

We perform calculations with equal, $SU(3)_f$ symmetric quark masses and extrapolate to the chiral limit $m_{u,d,s} \to 0$. The 10 $\mathcal{O}^{(ud)s}$ operators can then be further classified by the symmetry of the diquark factor [38] (see Table IV). Since the relevant operators are

$$\begin{aligned} \mathcal{O}^{3q}_{RR} &= \frac{1}{4}(\mathcal{O}^{3q}_{SS} + \mathcal{O}^{3q}_{SP} + \mathcal{O}^{3q}_{PS} + \mathcal{O}^{3q}_{PP}) = \mathcal{O}^{3q}_{+}, \\ \mathcal{O}^{3q}_{RL} &= \frac{1}{4}(\mathcal{O}^{3q}_{SS} - \mathcal{O}^{3q}_{SP} + \mathcal{O}^{3q}_{PS} - \mathcal{O}^{3q}_{PP}) = \mathcal{O}^{3q}_{-}, \end{aligned} \tag{50}$$

where R, L correspond to to $\Gamma^{(\prime)} = \frac{1}{2}(1 \pm \gamma_5)$, the only potential mixing is between operators $\{\mathcal{O}_{SS}, \mathcal{O}_{PP}, \mathcal{O}_{AA}\}$.

---

[5] It is worth noting that the complete conversion factors may also include perturbative corrections due to the quark fields depending on their renormalization scheme. In particular, the SMOM$_{\gamma_\mu}$ scheme that we use below requires $O(\alpha_S)$ correction comparable in magnitude to the one in Eq. (46), while SMOM and MOM do not.

[6] Operators with permuted quark fields can be reduced to the forms (48), (49) using Fierz identities.

TABLE IV. Classification of operators by parity and diquark symmetry [38]. Switching symmetry is determined by Γ; $\mathcal{S}(\Gamma = S, P, A) = -1$ and $\mathcal{S}(\Gamma = V, T) = +1$, while parity $\mathcal{P} = -\mathcal{P}(\Gamma)\mathcal{P}(\Gamma')$ is determined by both $\mathcal{P}(\Gamma^{(\prime)} = S, V, T) = +1$ and $\mathcal{P}(\Gamma^{(\prime)} = P, A, Q) = -1$.

	$\mathcal{S} = -1$	$\mathcal{S} = +1$
$\mathcal{P} = -1$	SS, PP, AA	VV, TT
$\mathcal{P} = +1$	SP, PS, AV	VA, TQ

Equivalently, one can study mixing and renormalization of operators $\{\mathcal{O}_{SP}, \mathcal{O}_{PS}, -\mathcal{O}_{AV}\}$, which is identical.[7] In the case of $\mathcal{O}^{(ud)d}$ operators, Fierz identities reduce the number of independent operators to the following four,

$$\mathcal{O}^{(ud)d}_{AA} = \mathcal{O}^{(ud)d}_{PP} - \mathcal{O}^{(ud)d}_{SS} = \mathcal{O}^{(ud)d}_{VV}, \tag{51}$$

$$\mathcal{O}^{(ud)d}_{AV} = \mathcal{O}^{(ud)d}_{SP} - \mathcal{O}^{(ud)d}_{PS} = \mathcal{O}^{(ud)d}_{VA}, \tag{52}$$

$$\mathcal{O}^{(ud)d}_{TT} = \mathcal{O}^{(ud)d}_{SS} + \mathcal{O}^{(ud)d}_{PP}, \tag{53}$$

$$\mathcal{O}^{(ud)d}_{TQ} = \mathcal{O}^{(ud)d}_{SP} + \mathcal{O}^{(ud)d}_{PS}, \tag{54}$$

and any potential mixing is respectively simplified.

The nonperturbative Green's functions are computed using quark propagators with point-sources and momentum-projected sinks in the Landau gauge,

$$S_q(x, p) = \sum_y e^{ip(x-y)} \langle q(x)\bar{q}(y)\rangle, \tag{55}$$

which are contracted at the source x (spin and color indices are omitted)

$$\begin{aligned} G^{3q}_{\Gamma\Gamma'}(x; p, k, r) = \sum_{y_1 y_2 y_3} & e^{iqx - ipy_1 - iky_2 - iry_3} \cdot \\ & \cdot \langle \mathcal{O}^{3q}_{\Gamma\Gamma'}(x)\bar{s}(y_3)\bar{d}(y_2)\bar{u}(y_1)\rangle, \end{aligned} \tag{56}$$

where $q = p + k + r$, and equivalently for the $\mathcal{O}^{(ud)d}$ operators. These Green's functions are then amputated with the same point source propagators after averaging over an entire ensemble,

TABLE V. Quark masses used for computing light and strange quark propagators for nonperturbative renormalization. The numbers of configurations used are shown in the second column.

Ensemble	$m_q^{\mathrm{NPR}(1)}$	N_{cfg}	$m_q^{\mathrm{NPR}(2)}$	N_{cfg}	$m_q^{\mathrm{NPR}(3)}$	N_{cfg}
24ID	0.00107	16	0.04	18	0.085	27
32ID	0.0001	22	0.02	0	.045	21

$$\begin{aligned} \Lambda^{(ud)s}_{\Gamma\Gamma'}(p, k, r) = & \langle\!\langle G^{(ud)s}_{\Gamma\Gamma'}(p, k, r)\rangle\!\rangle \cdot \\ & \cdot [\langle\!\langle S_s(r)\rangle\!\rangle^{-1} \langle\!\langle S_{u/d}(k)\rangle^{-1} \langle\!\langle S_{u/d}(p)\rangle\!\rangle^{-1}]. \end{aligned} \tag{57}$$

We evaluate 32 low-precision samples and one high-precision sample per configuration to correct for potential bias and use jackknife resampling to estimate statistical uncertainty. We perform these calculations with three values of equal quark masses $m_{u,d,s}$ varied between $m_{u/d}$ and m_s on each ensemble (see Table V). We observe very weak quark mass dependence in the diagonal renormalization constants. The figures below refer to the lightest quark mass, and final renormalization results are obtained by linear extrapolation with $m_{u,d,s} \to 0$. The only statistically significant mixing is observed between AA and PP operators, which vanishes towards the massless quark limit indicating that chiral symmetry is preserved (see Fig. 1).

The tree-level vertices of the three-quark operators $\mathcal{O}_{SS,PP,AA}$ have the following spin/color structure

$$\begin{aligned} [\Lambda^{3q}_{SS}]^{abc}_{\alpha\beta\gamma\delta} &= \epsilon^{abc}(C)_{\alpha\beta}(\mathbf{1})_{\gamma\delta}, \\ [\Lambda^{3q}_{PP}]^{abc}_{\alpha\beta\gamma\delta} &= \epsilon^{abc}(C\gamma_5)_{\alpha\beta}(\gamma_5)_{\gamma\delta}, \\ [\Lambda^{3q}_{AA}]^{abc}_{\alpha\beta\gamma\delta} &= \epsilon^{abc}(C\gamma_\mu\gamma_5)_{\alpha\beta}(\gamma_\mu\gamma_5)_{\gamma\delta}, \end{aligned} \tag{58}$$

and the corresponding projectors for the amputated Green's functions,

$$\begin{aligned} [P^{3q}_{SS}]^{abc}_{\alpha\beta\gamma\delta} &= \frac{1}{96}\epsilon^{abc}(C^{-1})_{\beta\alpha}(\mathbf{1})_{\delta\gamma}, \\ [P^{3q}_{PP}]^{abc}_{\alpha\beta\gamma\delta} &= \frac{1}{96}\epsilon^{abc}(\gamma_5 C^{-1})_{\beta\alpha}(\gamma_5)_{\delta\gamma}, \\ [P^{3q}_{AA}]^{abc}_{\alpha\beta\gamma\delta} &= \frac{1}{384}\epsilon^{abc}(\gamma_5\gamma_\mu C^{-1})_{\beta\alpha}(\gamma_5\gamma_\mu)_{\delta\gamma}, \end{aligned} \tag{59}$$

are used to form a 3 × 3 amputated Green's function matrix

$$\Lambda^{3q}_{XY}(p, k, r) = (\Lambda^{3q}_X(p, k, r)) \cdot P^{3q}_Y, \tag{60}$$

where $X, Y = \{SS, PP, AA\}$ and the dot indicates summation in all color and spin indices. From this matrix, the nonperturbative renormalization/mixing matrix Z^{3q}_{XY} is determined as

$$Z_q^{-3/2} Z^{3q}_{XY} \Lambda^{3q}_{YZ} = \delta_{XZ}. \tag{61}$$

The arrangement of momenta (p, k, r) defines a particular subtraction scheme for the three-quark operator; we will

---

[7] We note that discussion of renormalization and mixing is more natural in the spin-structure basis $\mathcal{O}_{SS}, \mathcal{O}_{PP}, \mathcal{O}_{AA}$, in which the symmetry constraints are straightforward. The results, however, are reported in the phenomenological "permutation" basis $\{(ud)s, (us)d, (sd)u\}_{RR,RL}$ (9). The latter basis is not orthogonal, which would complicate the pattern of nonperturbative mixing, e.g., due to chiral symmetry breaking by lattice discretization.

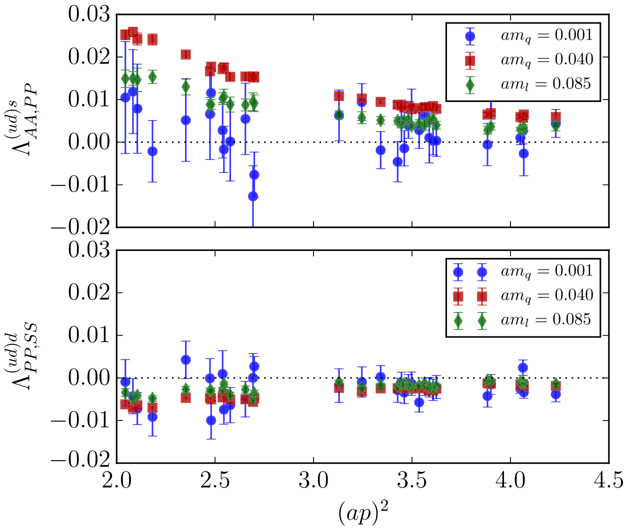

(a) 24ID

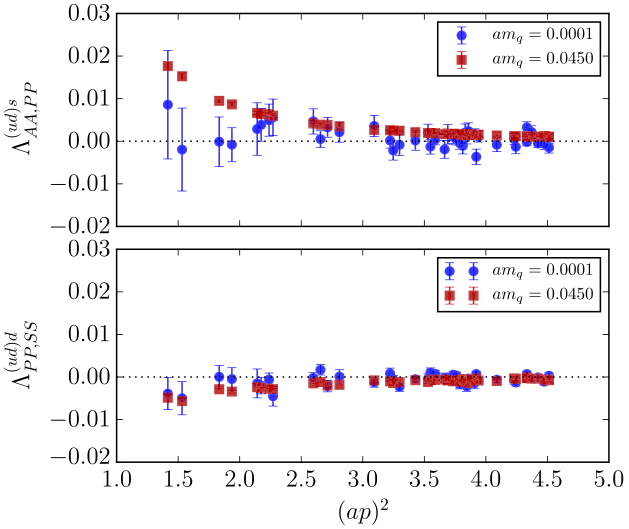

(b) 32ID

FIG. 1. Quark mass and scale dependence of the mixing Green's functions $\Lambda^{(ud)s}_{AA,PP}$ (top) and $\Lambda^{(ud)d}_{PP,SS}$ (bottom). Only two quark masses, the highest and the lowest, are shown for the 32ID ensemble.

use notation $|p|$ to indicate the subtraction point defining the scale. It is difficult to select lattice momenta satisfying the SMOM and SYM3q conditions exactly. We select momenta with the following criteria (1) p^2, k^2, r^2 values are within 10% of each other, and (2) p, k, r momenta satisfy the "democratic" orientation [67]

$$\frac{\sum_\mu p_\mu^4}{(\sum_\mu p_\mu^2)^2} \leq 0.4. \tag{62}$$

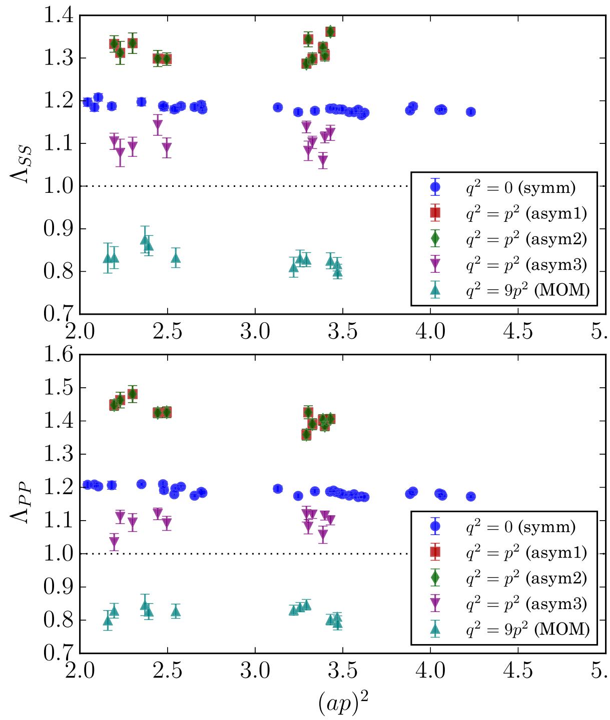

(a) 24ID

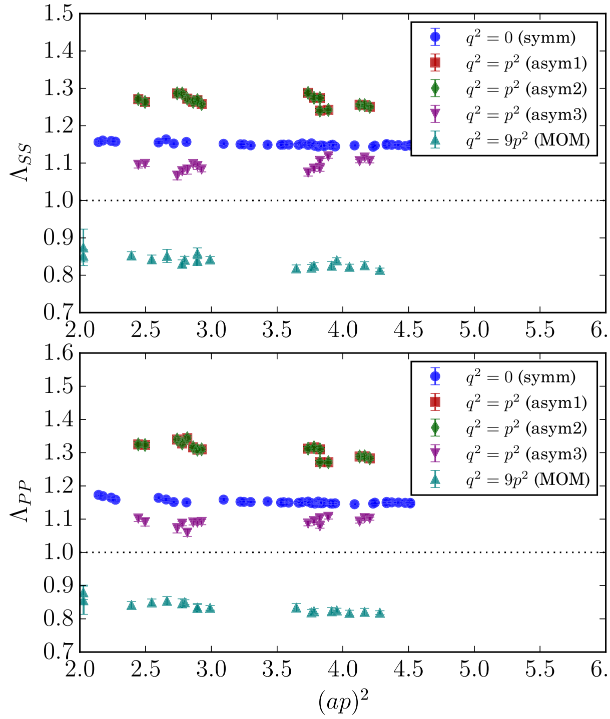

(b) 32ID

FIG. 2. Amputated Green's functions three-quark operators $\mathcal{O}^{(ud)s}_{SS}$ and $\mathcal{O}^{(ud)s}_{PP}$ with varying virtual momentum of the operator. Only diagonal entries (i.e., projected on SS and PP, respectively) are shown.

This ratio estimates the "diagonality" of the momentum, and the constraint avoids directions close to a single axis, which are expected to produce larger discretization effects. For the MOM and MOM3q schemes, we explore momenta along axes as well as 2-d, 3-d, and 4-d diagonals of the lattice. Wherever possible, amputated correlators are averaged over reflections and rotations of the external momenta.

In Fig. 2, we compare the amputated and projected Green's functions of the three-quark operators in MOM3q and SYM3q momentum schemes and find that they are different by $\approx 30\% - 35\%$. Although some difference is expected due to kinematics, it turns out to be substantially larger than expected from perturbative calculations (46), (47), which is $\approx 12\%$ at $|p| = 2$ GeV [see Eqs. (46) and (47)]. Since we observe only weak dependence of Green's functions on the momentum scale as $|p| \to 0$, this discrepancy is unlikely to be caused by nonperturbative effects such as a nucleon pole $(p^2 + m_N)^{-1}$, and may indicate large $O(\alpha_S^2)$ perturbative corrections in the MOM3q scheme. We have also briefly explored Green's functions in alternative schemes with quark momenta $p = \pm k = \pm r$ and $|p + k + r| = |p|$ ("asym1,2,3") shown in Fig. 2, which confirm the strong dependence of the vertex functions on the external quark momentum configuration. These observations validate our choice of the SYM3q scheme for renormalizing the three-quark operators.

To eliminate the quark field renormalization factor Z_q, we use Green's functions of quark axial-vector current

$$\Lambda_\Gamma(p, p') = \langle [\bar{q}\Gamma q] q(p) \bar{q}(p') \rangle_{\mathrm{amp}}. \tag{63}$$

with nonexceptional momenta $p^2 = p'^2 = (p - p')^2$. This Green's function is projected according to the "SMOM$_{\gamma_\mu}$" scheme,

$$\begin{aligned} Z_q^{\mathrm{SMOM}_{\gamma_\mu}}(|p|) &= [\Lambda_A]_{\mathrm{SMOM}_{\gamma_\mu}} Z_A^{WI} \\ &= \frac{1}{48} \sum_\mu \mathrm{Tr}[\gamma_5 \gamma_\mu \Lambda_{\gamma_\mu \gamma_5}] Z_A^{WI}. \end{aligned} \tag{64}$$

While such scheme is incompatible with the Ward identity for the axial current [62], it is more practical on a lattice because it does not depend on components of virtual external quark momenta and accompanying discretization effects. We use the values of the renormalization factors $Z_A^{WI} = 0.73457(11)$ (24ID) and 0.68779(11) (32ID) determined in Refs. [55,56] and perturbative calculations in the SMOM$_{\gamma_\mu}$ scheme [68] (see Appendix C for details). In Fig. 3, we show lattice renormalization constants of quark bilinears in the SMOM$_{\gamma_\mu}$ scheme

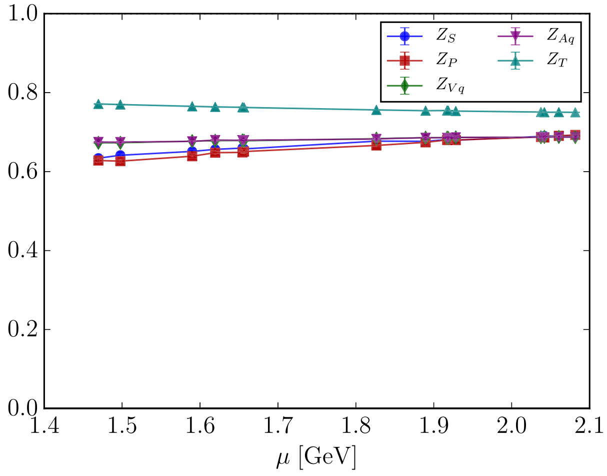

(a) 24ID

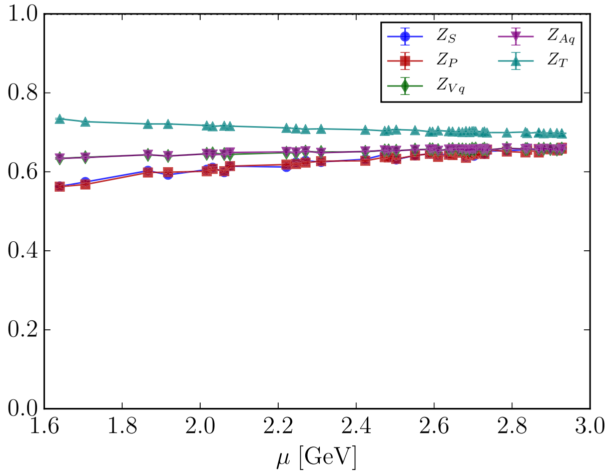

(b) 32ID

FIG. 3. Lattice renormalization factors of quark-bilinear operators (65) in the SMOM scheme.

$$Z_\Gamma = Z_A \frac{\Lambda_A^{\mathrm{SMOM}_{\gamma_\mu}}(|p|)}{\Lambda_\Gamma(|p|)}, \tag{65}$$

for $\Gamma = 1(S), \gamma_5(P), \gamma_\mu(V), \gamma_\mu\gamma_5(A), \sigma_{\mu\nu}(T)$ in Fig. 3.

Combining Eq. (61) with the axial-vector renormalization (64), we find the SYM3q renormalization matrix of three-quark operators

$$Z_{X,Y}^{\mathrm{lat}}(|p|) = [Z_A \Lambda_A(|p|)]^{3/2} [\Lambda^{3q}(|p|)]_{X,Y}^{-1}, \tag{66}$$

and show the results for the diagonal and off-diagonal components in Fig. 4. In previous calculations, MOM scheme with exceptional momenta was used to renormalize

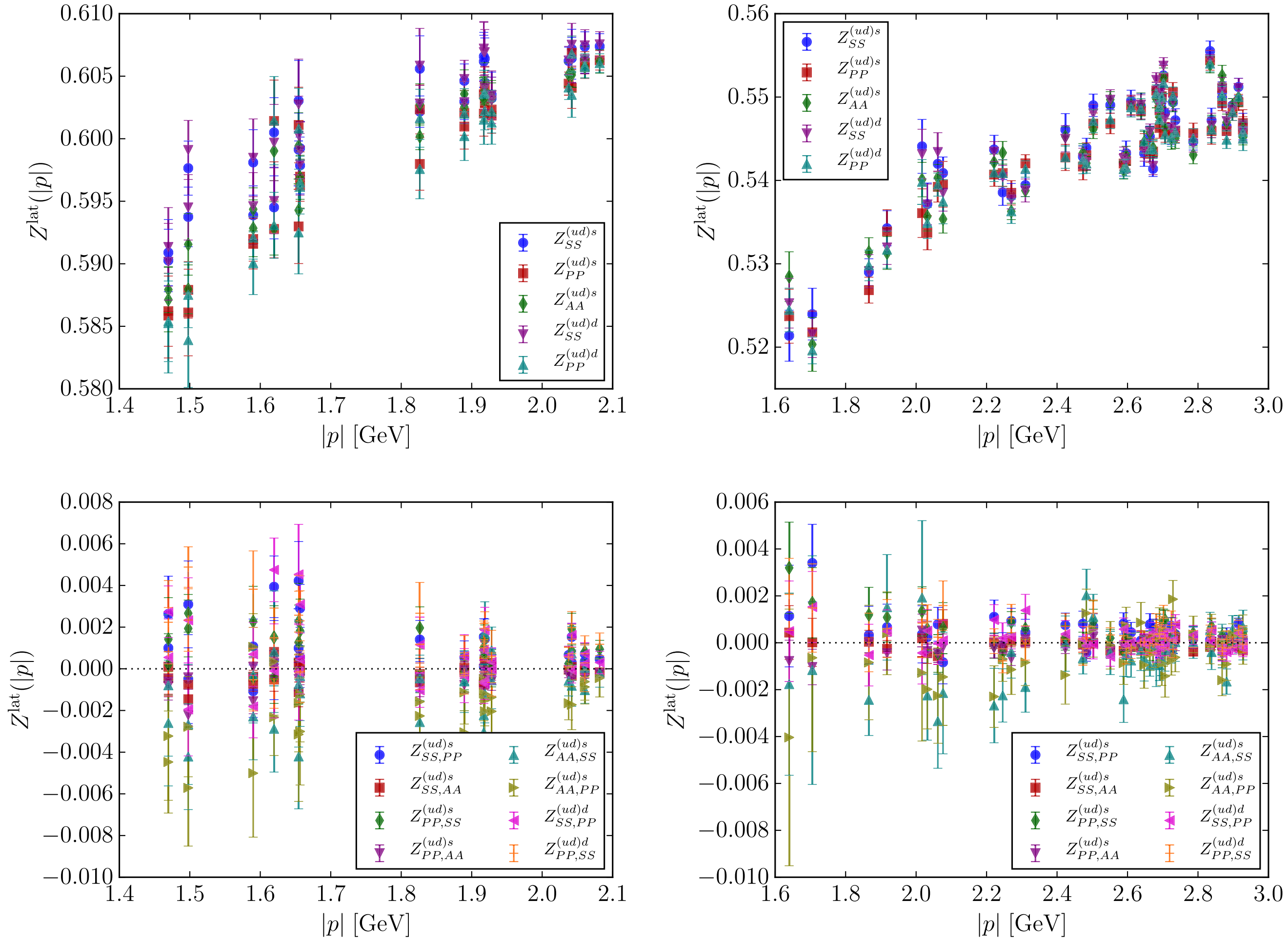

(a) 24ID (b) 32ID

FIG. 4. Diagonal renormalization (top) and off-diagonal mixing (bottom) components of the SYM3q renormalization matrix (66).

the quark fields. To emphasize the difference, we will refer to our scheme as SYM3q/SMOM$_{\gamma_\mu}$, and to the previously used scheme in Refs. [39,41,42] as MOM3q/MOM. All the off-diagonal components are negligible compared to the diagonal components. The most important observation is that mixing with the $\mathcal{O}^{3q}_{AA}$ operator may be neglected as its matrix elements have not been computed. Below, we study only the diagonal factors $Z_{X,X}$ and refer to them simply as Z_X for $X = SS, PP, AA$.

C. Perturbative matching

In order to extract lattice to $\overline{\rm MS}$-conversion coefficients, we divide SYM3q/SMOM$_{\gamma_\mu}$ renormalization factors (66) by their perturbative evolution. Specifically, we use continuum-QCD conversion factor from SYM3q/SMOM$_{\gamma_\mu}$ scheme with $N_f = 3$ flavors at the momentum-subtraction point $|p|$ to our final $\overline{\rm MS}$ scheme with $N_f = 4$ flavors at scale $\mu_0 = 2$ GeV,

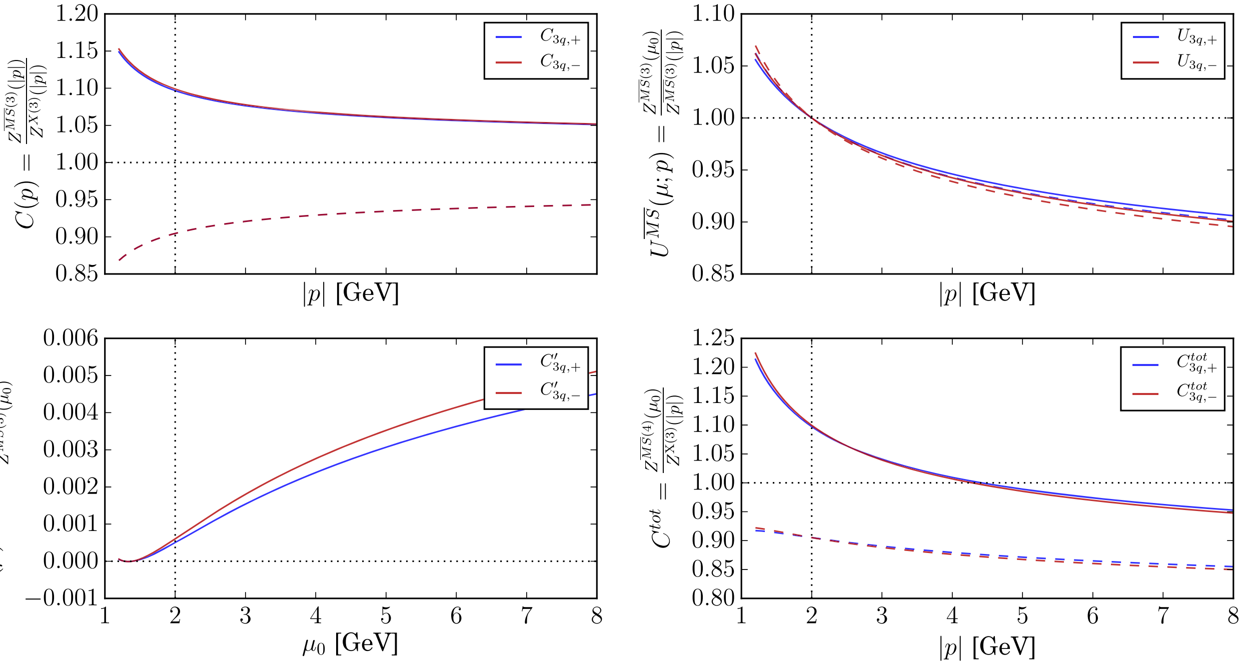

FIG. 5. (Top left) perturbative running and conversion from SYM3q/SMOM$_{\gamma_\mu}$ (solid lines) and MOM3q/MOM (dashed lines) to $\overline{\mathrm{MS}}$ scheme at scale $|p|$; (top right) $\overline{\mathrm{MS}}$ running from scale $|p|$ to $\mu_0 = 2$ GeV at $O(\alpha_S^3)$ used in this work (solid) and $O(\alpha_S^2)$ used previously (dashed); (bottom left) conversion from $N_f = 3$ to $N_f = 4$ flavors; (bottom right) all factors collected (67).

$$C^{\mathrm{tot}}(\mu_0;|p|) = \frac{Z^{\overline{\mathrm{MS}}(4)}(\mu_0)}{Z^{\mathrm{SYM3q/SMOM}_{\gamma_\mu}(3)}(|p|)} = \left(\frac{Z^{\overline{\mathrm{MS}}(4)}(\mu_0)}{Z^{\overline{\mathrm{MS}}(3)}(\mu_0)}\right)\cdot \cdot\left(\frac{Z^{\overline{\mathrm{MS}}(3)}(\mu_0)}{Z^{\overline{\mathrm{MS}}(3)}(|p|)}\right)\cdot\left(\frac{Z^{\overline{\mathrm{MS}}}(|p|)}{Z^{\mathrm{SYM3q/SMOM}_{\gamma_\mu}}(|p|)}\right), \tag{67}$$

where the last factor is computed with $N_f = 3$ flavors as summarized in Appendix C.

Since there is perturbative mixing between SS and PP operators starting at $O(\alpha_S^2)$, the anomalous dimension matrix has to be diagonalized. This results in two different anomalous dimensions $\gamma_\pm$ for operators (50) [63,65].[8] We integrate these $O(\alpha_S^3)$ anomalous dimensions [63] using the four-loop $\alpha_S^{\overline{\mathrm{MS}}}(\mu)$ running derived from $\alpha_S^{\overline{\mathrm{MS}}}(M_Z) = 0.11823(81)$ and matched to the $N_f = 3$ QCD at $\bar{m}_b$ and $\bar{m}_c$ thresholds [69]. The complete conversion factor is shown in Fig. 5, as well as all the factors separate factors in the right-hand side of Eq. (67). The correction from $N_f = 3$ dynamical flavors used in lattice calculations to $N_f = 4$ active flavors at scale μ_0 is smaller than 10^{-3} and thus may be neglected. Also, the difference in evolution of operator normalization with $O(\alpha_S^2)$ and $O(\alpha_S^3)$ anomalous dimensions are very small. Finally, we compare the complete conversion factors in the SYM3q/SMOM$_{\gamma_\mu}$ and MOM3q/MOM schemes in Fig. 5 (bottom right). The α_S and α_S^2 orders contribute respectively ≈7.1% and ≈2.6% to perturbative SYM3q → $\overline{\mathrm{MS}}$ conversion factors [63], and we estimate the perturbative systematic uncertainty as half of the $O(\alpha_S^2)$ contribution at ≈1.3%. Such uncertainty is negligible compared to uncertainties from other sources, in particular, stochastic and discretization effects.

Conversion factors from lattice to $\overline{\mathrm{MS}}(N_f = 4, \mu_0)$ are products of the perturbative running (67) and lattice renormalization factor (66) in the $\mathcal{O}_\pm$ basis (50)

$$Z^{\overline{\mathrm{MS}}\leftarrow\mathrm{lat}}(\mu_0;|p|) = C^{\mathrm{tot}}(\mu_0;|p|)Z^{\mathrm{lat}}(|p|), \tag{68}$$

which should be scale independent of the intermediate scale $|p|$ within the window (45). Indeed, as shown in Fig. 6, the variation of $Z^{\overline{\mathrm{MS}}\leftarrow\mathrm{lat}}(\mu_0;|p|)$ with the lattice scale $|p|$ is insignificant compared to our target precision. Final renormalization numbers are determined as simple averages of central values in the range $|p| = 1.8\ldots2.1$ GeV for both ensembles. While data at larger scales are available for the 32ID ensemble, we use the same scale window in physical units to ensure consistency of our continuum extrapolation below. The systematic uncertainties are estimated as half of the maximal variation in the averaging range, and are subdominant compared to the perturbative uncertainty discussed above;

---

[8] Using parity, we take the average the opposite chirality operators $\mathcal{O}_+ = \frac{1}{2}(\mathcal{O}_{RR} + \mathcal{O}_{LL})$ and $\mathcal{O}_+ = \frac{1}{2}(\mathcal{O}_{LR} + \mathcal{O}_{RL})$.

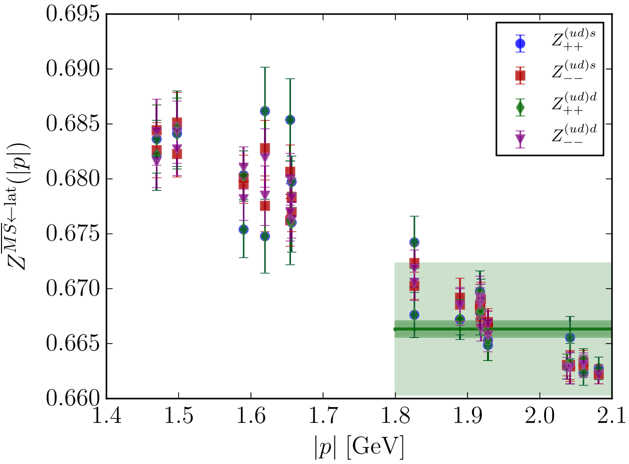

(a) 24ID

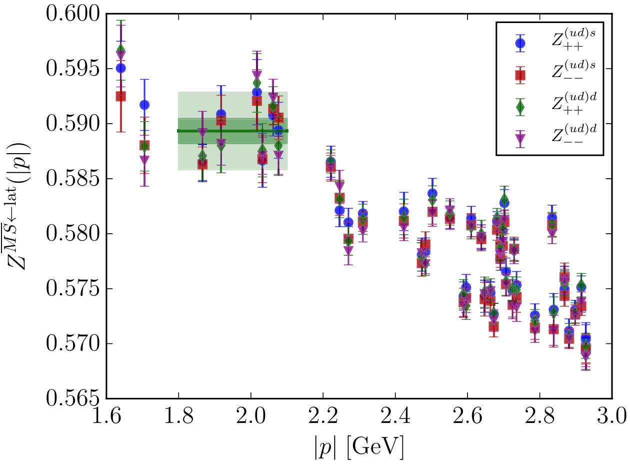

(b) 32ID

FIG. 6. Diagonal conversion factors from SYM3q/SMOM$_{\gamma_\mu}$ to $\overline{\text{MS}}(2\text{ GeV})$ scheme (68), in which perturbative running with intermediate scale $|p|$ has been removed. In absence of discretization, nonperturbative, and higher-order perturbative effects, it should be independent of $|p|$. The green bands indicate averages over the same momentum range on both ensembles, which is necessary for consistent continuum extrapolation.

combined systematic uncertainties are $\lesssim 1.6\%$. The statistical uncertainties are estimated with jackknife resampling and are $\lesssim 0.2\%$. The final renormalization constants are collected in Table VI.

IV. RESULTS

A. Hadron spectrum

The first step of the analysis is to extract energies of proton and meson states and their overlaps with the lattice operators from their two-point correlators. We perform multi-state fits in order to control systematic effects arising from hadron excited states. Statistical precision of our data and coarse step in the time direction are sufficient to constrain effectively only one excited state in each case. Energy gaps between the ground and the excited state have the most impact on correct removal of excited-state contamination from matrix elements determined from three-point correlation functions.

To find approximate values of the ground state parameters, we first perform 1-state fits with t_{min} sufficiently large to yield good p-values for all momenta $p^2 = (0\ldots4)\times(2\pi/L)^2$. We then perform series of two-state fits (32), (33) with varying time ranges $[t_{\text{min}}, t_{\text{max}}]$. We use values of the ground-state overlaps C_0 and the energies E_0 from the one-state fits with $t_{\text{min}} = 6a$ for 24ID and $t_{\text{min}} = 7a$ for 32ID to impose Gaussian prior constraints in order to stabilize the two-state fits. To ensure that these priors are noninformative, we set their normal widths equal to $(3\ldots5)\times$ their statistical uncertainties in the one-state fits. In addition, we impose priors on the energy gap ΔE_1 with a wide log-normal prior distribution

$$\begin{aligned} p_{\log\text{-N}}(\Delta E_1) &= \exp\left[-\frac{1}{2}P_{\log\text{-N}}(\Delta E_1)\right] \\ &= \exp\left[-\frac{1}{2\lambda_{\Delta E_1}}\left(\log\frac{\Delta E_1}{\widetilde{\Delta E_1}}\right)^2\right], \qquad (69) \end{aligned}$$

with the mode $\widetilde{\Delta E_1} = 0.5\text{ GeV}$ and the log-width $\lambda_{\Delta E_1} = 3$. We also impose constraints on the excited-state overlaps $C_1 > 0$, since the source and the sink operators are the same.

To perform the fits, we use the "augmented" $\tilde{\chi}^2$ function

$$\begin{aligned} \tilde{\chi}^2 &= \chi^2 + \sum_k P_k(p_k), \\ \chi^2 &= \sum_{t,t'}(y_t - \tilde{C}_{2pt}(t))S^{-1}_{t,t'}(y_{t'} - \tilde{C}_{2pt}(t')), \qquad (70) \end{aligned}$$

TABLE VI. Final renormalization factors from lattice to $\overline{\text{MS}}(N_f = 4, \mu = 2\text{ GeV})$ with statistical (1), and systematic uncertainties from momentum scale (2) and perturbative matching (3).

	$Z^{(ud)s}_{++}$	$Z^{(ud)s}_{--}$	$Z^{(ud)d}_{++}$	$Z^{(ud)d}_{--}$
24ID	0.6671(7)(60)(87)	0.6674(7)(51)(87)	0.6671(7)(60)(87)	0.6672(7)(49)(87)
32ID	0.5895(11)(32)(77)	0.5896(9)(29)(77)	0.5893(11)(33)(77)	0.5897(9)(36)(77)

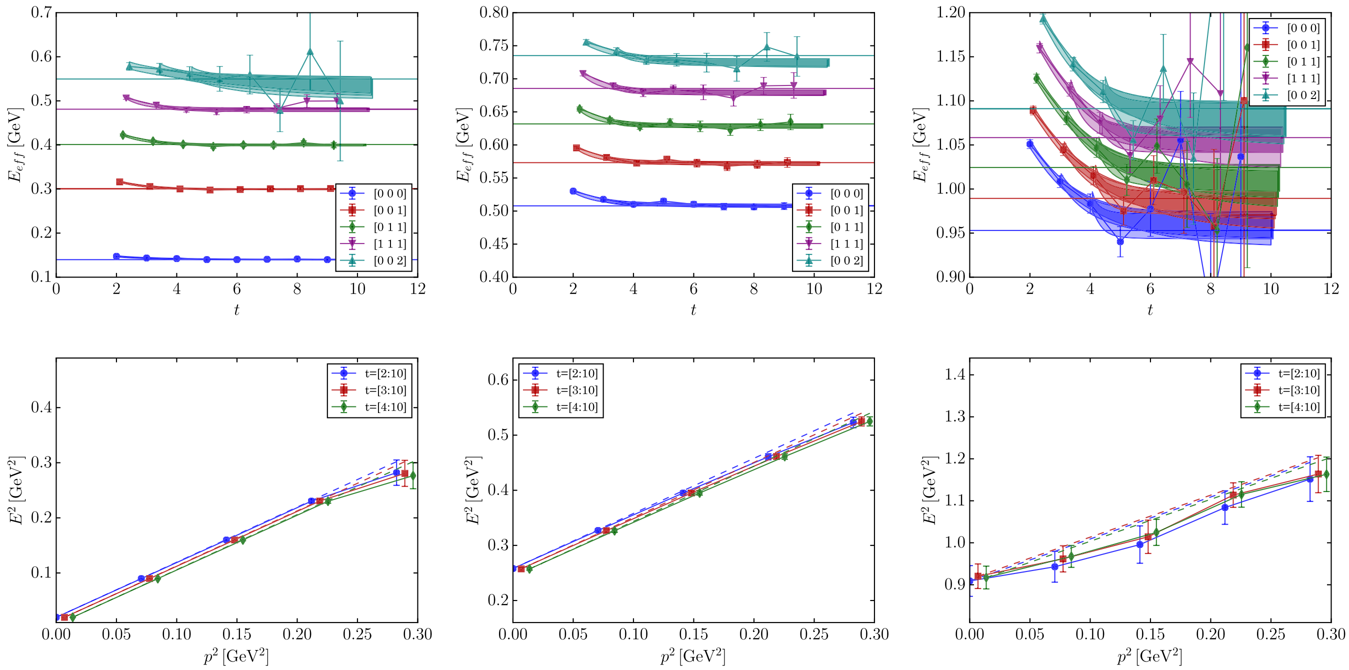

(a) Pion (b) Kaon (c) Nucleon

FIG. 7. Two-state fits to pion, kaon, and nucleon two-point correlation functions shown as effective energies (top) and ground-state dispersion relations (bottom) on the 24ID ensemble. The continuum dispersion relations $E^2(p) = E^2(0) + p^2$ for ground-state energies are shown with horizontal lines in the top panels and with dashed lines in the bottom panels.

where $P_k(p_k)$ are log-likelihood weights of the prior constraints imposed on parameters p_k, and the regular χ^2 is computed with the sample covariance matrix S. The fits are performed by minimizing this “augmented least-squares” with trusted-region Levenberg-Marquardt algorithm.

The fits for pion, kaon, and nucleon at all relevant momenta are summarized in Figs. 7 and 8. In the bottom panels, we compare the resulting energies $E^2(p^2)$ to the continuum dispersion relation $E^2 = m^2 + p^2$ using masses $m = E(0)$ obtained on the lattice. Uncertainties in all fits are estimated using bootstrap resampling with $N_{\mathrm{boot}} = 256$ samples.

The kaon correlation functions are the most statistically precise and their two-state fits exhibit remarkable consistency between fits with $t_{\mathrm{min}} = (2\ldots4)a$ on 24ID and $t_{\mathrm{min}} = (2\ldots3)a$ on 32ID ensembles; the corresponding ground-state energies align perfectly with the continuum dispersion relation. We observe that the pion correlation functions are less statistically precise, and they display especially large fluctuations at the largest momentum (0, 0, 2). Most likely, this indicates that our scheme for approximating light-quark propagators, the low-eigenmode deflation combined with the truncated conjugate-gradient, does not perform equally well for high-momentum light hadron states, compared to low-momentum ones. Fortunately, since the high-momentum pion data are used only in one of the three kinematic points, their statistical fluctuations have only small adverse effect on the final results. For all the lower momenta, the data are precise, the fits are stable, and their agreement with the continuum dispersion relation is remarkable. The nucleon data are the least precise and the fits show some dependency on the fitting range. On the 24ID ensemble, all fits with $t_{\mathrm{min}} = (2\ldots4)$ produce consistent results that agree with the continuum dispersion relations. On the 32ID ensemble, however, the results at some of the momenta depend on the fit range, albeit within statistical fluctuations. We attribute this difference to over smearing of the light-quark propagator sources on the 32ID ensemble, where the larger statistical fluctuations make it difficult to constrain the smaller excited-state contributions and specifically their energy gaps. Although suppressing excited-state contributions is generally advantageous, poorly constrained energy gaps may lead to larger fluctuations in the ground state matrix elements to be determined in the next step. For subsequent fitting of the three-point functions on both 24ID and 32ID ensembles, we select parameters from two-state fits with $t_{\mathrm{min}} = 2a$, which all have satisfactory p-values. These energies are collected in Table VII.

Since we use the sample covariance matrix that may be poorly determined, assessing the fit quality with the usual χ^2 distribution may be misleading. Instead, we judge the quality of the fits in two ways: (a) as p-values computed from the Hotelling distributions of the optimal “χ^2” values, and (b) using empirical cumulative distribution of “χ^2”

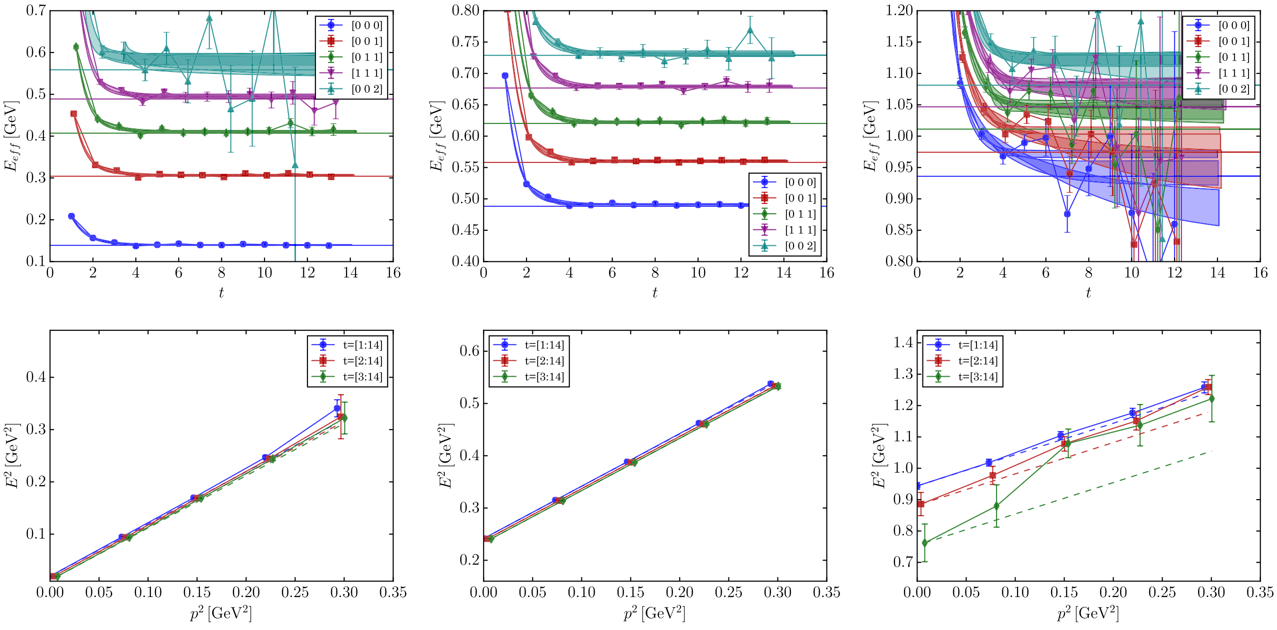

(a) Pion (b) Kaon (c) Nucleon

FIG. 8. Two-state fits to pion, kaon, and nucleon two-point correlation functions shown as effective energies (top) and ground-state dispersion relations (bottom) on the 32ID ensemble. See caption to Fig. 7 for description.

computed with bootstrap variation of the data around the optimal fit curve as detailed in Ref. [70]. Since the prior constraints are used only to stabilize the search of the optimal point, they are not included in computing the "χ^2" or the number of degrees of freedom.

B. Proton decay form factors

Values of the proton decay form factors W_0 and W_1 are extracted from the three-point correlation functions (19) as follows:

1. The projected lattice three-point functions (20) are fitted to the two-state Ansatz (40) with proton and meson ground and excited state energies fixed at values determined in the two-point function fits described above. This linear fit yields nucleon-meson decay matrix elements up to the hadron-operator normalization factors $Z_{N,\Pi}$, which are also determined from the two-point function fits.
2. Form factors $W_{0,1}(Q^2)$ are computed From the ground-state matrix elements, at three kinematic points.
3. On each ensemble, form factor data are interpolated to the points $Q_e^2 = -m_e^2 \approx 0$ and $Q_\mu^2 = -m_\mu^2$ that correspond to the $N \to \Pi e$ and $N \to \Pi\mu$ decays, respectively (see Fig. 11).
4. At each physical-decay kinematic point $Q_{\mu,e}^2$, linear extrapolations in a^2 are performed to obtain the continuum-limit value (also shown in Fig. 11).

Due to the coarse lattice spacings, the fit ranges resulting in stable fits of the excited state energy are very limited. We find that nucleon and meson excitation energies ΔE_1 obtained from fits with $t_{\min} = 2$ lead to the most robust fits of the three-point functions on both ensembles. In order to minimize excited state effects in the three-point functions, we omit $t_{\rm skip}^N = 2$ points at the proton source and $t_{\rm skip}^\Pi = 4$ points at the meson sink, although results are stable with respect to

TABLE VII. Ground-state energies of the pion, the kaon, and the nucleon extracted from the two-state fits of the two-point functions with $t_{\min} = 2$ and used in three-point function fits. The columns correspond hadron momenta $p^2 = (2\pi/L)^2 n^2$.

		$n^2 = 0$	$n^2 = 1$	$n^2 = 2$	$n^2 = 3$	$n^2 = 4$
24ID	π	0.13983(72)	0.29951(95)	0.3997(18)	0.4799(39)	0.531(22)
	K	0.5079(25)	0.5719(28)	0.6285(33)	0.6788(41)	0.7232(66)
	n	0.953(19)	0.971(19)	0.998(22)	1.041(19)	1.073(25)
32ID	π	0.13889(68)	0.3049(11)	0.4085(19)	0.4913(41)	0.566(37)
	K	0.48817(76)	0.55725(78)	0.61868(97)	0.6746(15)	0.7260(30)
	n	0.936(20)	0.983(15)	1.032(11)	1.067(13)	1.115(11)

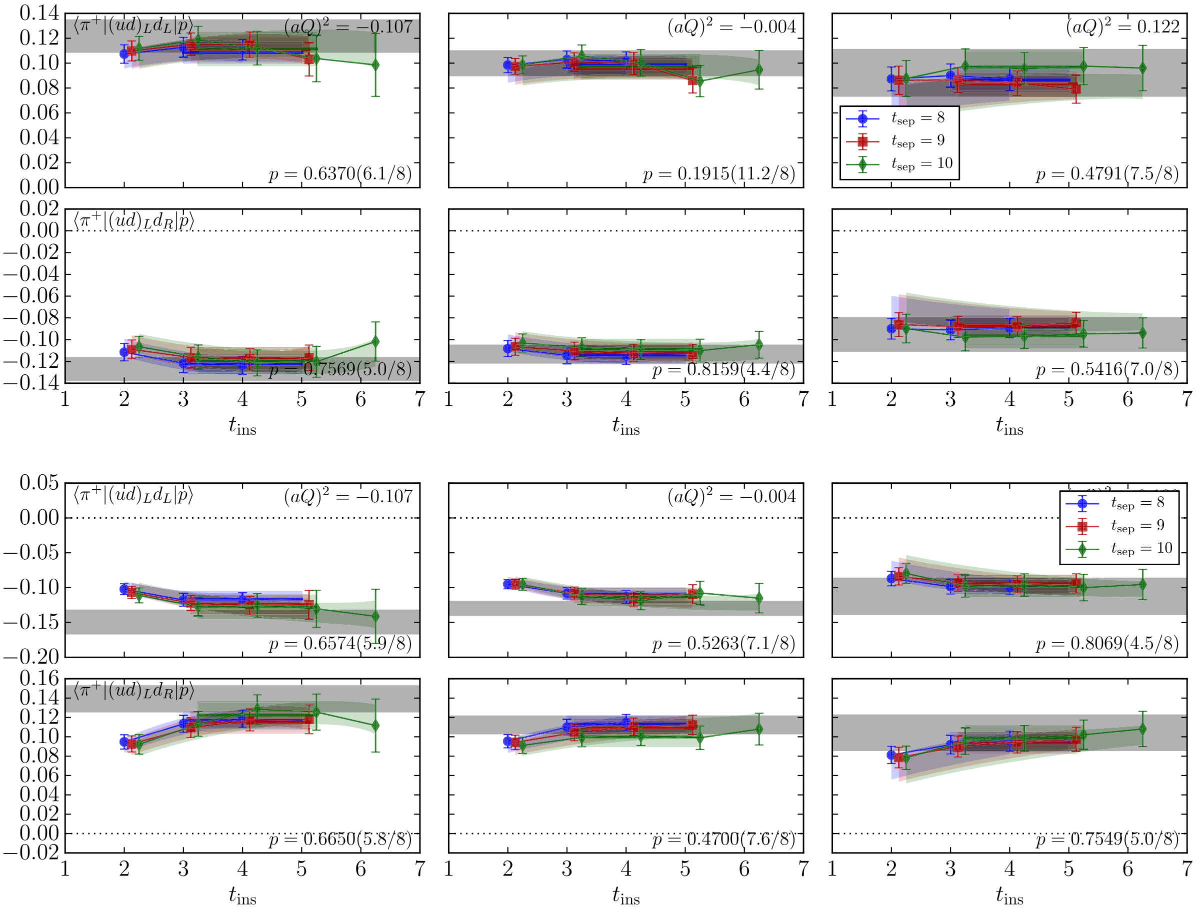

FIG. 9. Two-state fits of renormalized $N \to \pi$ correlation functions for form factor W_0 (top) and W_1 (bottom) at the three kinematic points on the 24ID lattices with $a \approx 0.20$ fm. The data points show the ratio (39) and the bands show the corresponding fit functions as described in the text. The horizontal gray bands represent ground-state form factor values. All error bars are statistical and evaluated using bootstrap. Fit quality (p-value) is estimated using the Hotelling distribution.

varying these numbers by ±1. To avoid unrealistic large fluctuations in χ^2 values and fit parameters, the covariance matrix for the fit is "shrunk" to its diagonal part

$$\tilde{S}(\lambda) = (1-\lambda)S + \lambda\,\mathrm{diag}(S), \qquad (71)$$

with "shrinkage" parameter $\lambda = 0.1$. This is necessary due to strong correlations of data with different t_2 that lead to poorly-conditioned correlation matrices with eigenvalues as small as 10^{-5}.

In each channel and at each momenta, we study two projections [(42) and (44)], from which the two form factors $W_{0,1}$ factors are computed directly. Using parity, we take the average the left- and right-handed matrix elements, i.e., LL with RR, and LR with RL.[9] Separate fits are performed independently for all channels and kinematic points. In Figs. 9 and 10 we show example results of these fits in terms of the form factor $W_{0,1}$ values in the $\overline{\rm MS}(2~{\rm GeV})$ scheme and using physical units GeV^2 (fit figures for other channels and ensembles are enclosed as Supplemental Materials [71]). The time-dependent "ratio" data points are computed using Eq. (39), and the plateau averages are computed over $t_1 = (3\ldots5)a$. To examine the agreement between the data and the fits, we also show similar ratios reconstructed from the fit functions (34), (35), (40). In each panel, we also show Hotelling p-values along with the respective values of $\chi^2/\mathrm{d.o.f.}$ we use to assess the fit quality.

We observe close agreement between the plateau and the ground-state fit values indicating that excited-state contributions are negligible. The statistical uncertainties of the ground-state fit values are close to those of the plateau values at the largest source-sink separation and are thus conservative. In channels with the final state $\pi(0,0,2)$ on the 24ID ensemble, fluctuations are larger due to the larger uncertainty in the corresponding two-point functions. Systematic uncertainties due to excited states

---

[9] On the 24ID ensemble, the precision of the AMA approximation is different for the left-handed and right-handed components due to the asymmetric zMöbius-action coefficients in the fifth dimension. To accommodate that, we compute the average of the left- and right-handed matrix elements weighted with $\propto \sigma^{-2}$, where σ is the statistical fluctuation.

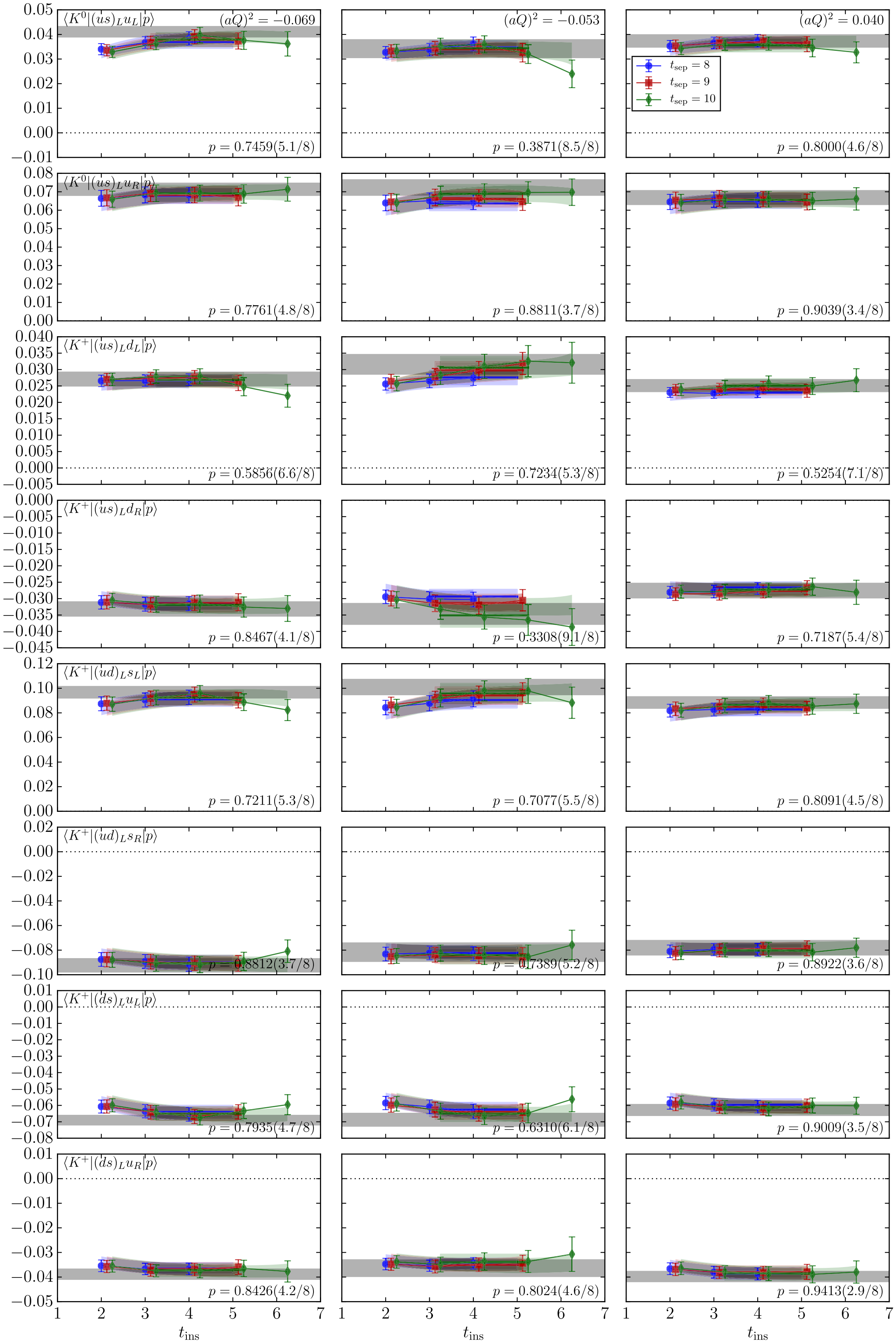

FIG. 10. Two-state fits of the $N \to K$ form factor W_0 on 24ID. For explanation, see caption to Fig. 9.

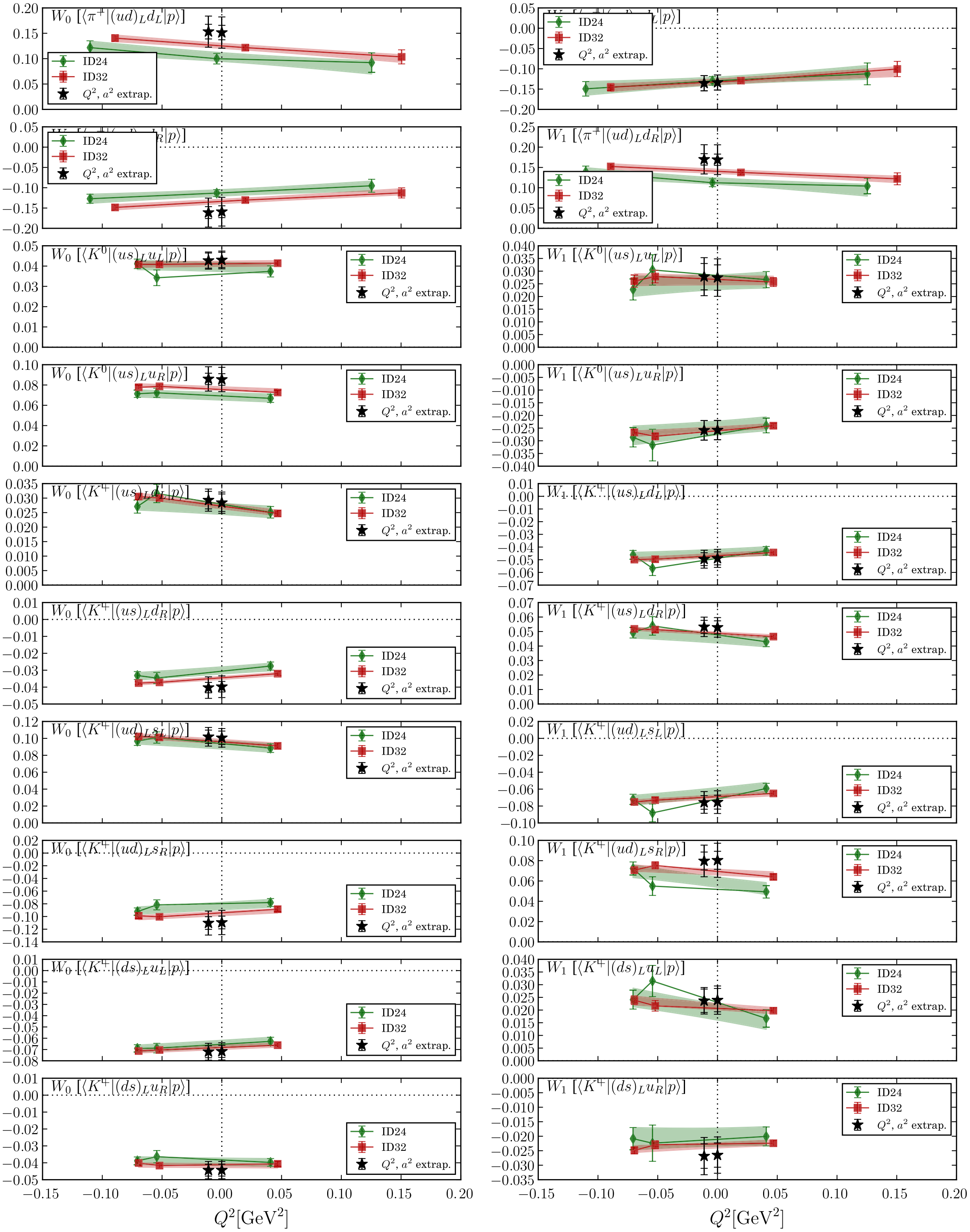

FIG. 11. Linear interpolation of form factor data to the decay kinematic points $Q^2 = -m_e^2 \approx 0$ and $Q^2 = -m_\mu^2$ (bands) for W_0 in the left column and W_1 in the right column followed by continuum extrapolation in a^2 (black stars). The 24ID and 32ID lattice data are shown with statistical uncertainties only, and the final extrapolated results are shown with statistical (smaller error bars) and the total (larger error bars) uncertainties including those from excited states and the continuum limit extrapolation as described in the text.

TABLE VIII. Results for the form factors $W_{0,1}$ on the two ensembles and in the continuum limit at the two kinematic points $Q^2 = 0$ (first line) and $Q = -m_\mu^2$ (second line) renormalized to $\overline{\mathrm{MS}}(2\ \mathrm{GeV})$. The first uncertainty is statistical, the second is systematic due to excited states, and the third is the uncertainty of the continuum extrapolation.

	$W_0[\mathrm{GeV}^2]$		
	24ID	32ID	Cont.
$\langle\pi^+|(ud)_L d_L|p\rangle$	0.1032(86)(26)	0.1252(48)(50)	0.151(14)(8)(26)
	0.1050(87)(36)	0.1271(49)(50)	0.153(14)(7)(26)
$\langle\pi^+|(ud)_L d_R|p\rangle$	−0.1125(78)(41)	−0.134(5)(11)	−0.159(15)(20)(25)
	−0.1139(78)(45)	−0.136(5)(12)	−0.161(15)(20)(26)
$\langle K^0|(us)_L u_L|p\rangle$	0.0395(22)(36)	0.0411(13)(25)	0.0430(38)(12)(19)
	0.0397(22)(36)	0.0411(13)(25)	0.0427(37)(12)(16)
$\langle K^0|(us)_L u_R|p\rangle$	0.0688(37)(19)	0.0764(17)(36)	0.0854(57)(55)(90)
	0.0693(36)(20)	0.0769(17)(36)	0.0860(56)(55)(91)
$\langle K^+|(us)_L d_L|p\rangle$	0.0263(19)(6)	0.0273(9)(11)	0.0284(30)(17)(12)
	0.0266(19)(6)	0.0278(9)(11)	0.0293(30)(18)(15)
$\langle K^+|(us)_L d_R|p\rangle$	−0.0301(21)(10)	−0.0345(9)(14)	−0.0398(31)(20)(52)
	−0.0307(21)(10)	−0.0351(8)(15)	−0.0403(31)(20)(52)
$\langle K^+|(ud)_L s_L|p\rangle$	0.0923(48)(35)	0.0961(26)(46)	0.1006(80)(60)(46)
	0.0932(47)(37)	0.0972(26)(48)	0.1019(79)(60)(47)
$\langle K^+|(ud)_L s_R|p\rangle$	−0.0835(58)(3)	−0.0954(32)(39)	−0.109(10)(8)(14)
	−0.0846(58)(6)	−0.0964(32)(40)	−0.110(10)(8)(14)
$\langle K^+|(ds)_L u_L|p\rangle$	−0.0651(33)(26)	−0.0681(18)(33)	−0.0717(54)(41)(35)
	−0.0658(32)(28)	−0.0686(18)(34)	−0.0720(53)(40)(34)
$\langle K^+|(ds)_L u_R|p\rangle$	−0.0394(22)(20)	−0.0417(11)(23)	−0.0443(35)(26)(27)
	−0.0393(21)(21)	−0.0416(11)(23)	−0.0444(35)(26)(27)

	$W_1[\mathrm{GeV}^2]$		
	24ID	32ID	Cont.
$\langle\pi^+|(ud)_L d_L|p\rangle$	−0.130(10)(17)	−0.1316(67)(82)	−0.134(18)(2)(2)
	−0.132(10)(17)	−0.1335(67)(81)	−0.136(19)(3)(2)
$\langle\pi^+|(ud)_L d_R|p\rangle$	0.116(8)(11)	0.140(5)(14)	0.169(14)(18)(29)
	0.118(8)(12)	0.142(5)(15)	0.170(14)(18)(28)
$\langle K^0|(us)_L u_L|p\rangle$	0.0256(29)(4)	0.0264(18)(22)	0.0275(50)(53)(10)
	0.0254(29)(4)	0.0265(19)(22)	0.0278(52)(52)(13)
$\langle K^0|(us)_L u_R|p\rangle$	−0.0250(27)(30)	−0.0253(9)(18)	−0.0258(38)(3)(4)
	−0.0254(28)(31)	−0.0256(9)(19)	−0.0259(38)(4)(2)
$\langle K^+|(us)_L d_L|p\rangle$	−0.0448(30)(13)	−0.0467(17)(27)	−0.0489(51)(44)(22)
	−0.0453(30)(16)	−0.0472(16)(28)	−0.0496(51)(43)(23)
$\langle K^+|(us)_L d_R|p\rangle$	0.0452(31)(23)	0.0487(10)(25)	0.0529(45)(28)(42)
	0.0458(31)(23)	0.0492(10)(26)	0.0532(45)(29)(40)
$\langle K^+|(ud)_L s_L|p\rangle$	−0.0638(54)(24)	−0.0691(23)(52)	−0.0754(82)(86)(63)
	−0.0653(54)(32)	−0.0701(23)(55)	−0.0757(80)(82)(57)
$\langle K^+|(ud)_L s_R|p\rangle$	0.0588(50)(11)	0.0687(28)(43)	0.080(9)(8)(12)
	0.0605(50)(15)	0.0693(28)(43)	0.080(9)(8)(10)
$\langle K^+|(ds)_L u_L|p\rangle$	0.0192(31)(15)	0.0213(13)(16)	0.0239(46)(18)(26)
	0.0201(31)(19)	0.0217(13)(17)	0.0237(46)(15)(19)
$\langle K^+|(ds)_L u_R|p\rangle$	−0.0203(31)(5)	−0.0231(9)(12)	−0.0265(42)(32)(34)
	−0.0204(31)(7)	−0.0233(9)(12)	−0.0269(42)(33)(35)

are conservatively estimated from the differences between values obtained from the fits and the plateau averages at the largest source-sink separation $t_2 = 10a$. These systematic errors are propagated forward to the final Q^2- and continuum-extrapolated results.

Using data at the three kinematic points, we perform linear interpolation in Q^2 to obtain values at $Q^2 = -m_e^2 \approx 0$ and $Q^2 = -m_\mu^2$. The decay-kinematic data points are then extrapolated to the continuum limit as $W(a) \sim W^{\mathrm{cont}} + W' a^2$. Such expected scaling of discretization errors is justified by the automatic $O(a^2)$ improvement due to chiral symmetry of the fermion action. Having only two values of the lattice spacing, it is impossible to estimate systematic uncertainty of such extrapolation in a robust way; therefore, we resort to a conservative estimate from the discrepancy between the continuum-extrapolated results and the results from the finer 32ID ensemble. The momentum interpolations are shown in Fig. 11 for both ensembles, together with the final continuum-extrapolated values. The individual lattice data points and their Q^2 fit bands are shown only with statistical uncertainties, while the extrapolated values are shown with statistical and total uncertainties. The latter include systematic uncertainties due to the excited states and the continuum extrapolation.

Our final results for both form factors W_0 and W_1 are collected in Table VIII. For completeness, we include values on both ensembles as well as their continuum-extrapolated values. We quote separate statistical, excited-state and continuum-extrapolation systematic uncertainties where appropriate.

C. Proton decay amplitudes

In this section, we present our determination of proton decay constants (16). Combined with phenomenological constants D and F from spin physics, these parameters yield leading-order ChPT estimates of proton-meson decay amplitudes (see Appendix B).

We determine the proton decay constants from the two-point correlation functions of the proton creation and proton decay operators,

$$C_+^{\mathcal{O}\bar{N}}(\vec{k},t) = \sum_{\vec{x}} e^{-i\vec{k}\vec{x}} \frac{(1+\gamma_4)_{\beta\alpha}}{2} \langle \mathcal{O}_\alpha(\vec{x},t)\bar{N}(0)\rangle \overset{t\to\infty}{=} \frac{f_N}{\sqrt{Z_N(\vec{k})}} C_+^{N\bar{N}}(\vec{k},t), \qquad (72)$$

where $f_N = \{\alpha,\beta\}$ for $\mathcal{O} = \mathcal{O}_{RL,LL}^{(ud)u}$, respectively. We extract these constants using the ratio

$$R^{\mathcal{O}\bar{N}}(\vec{k},t) = \sqrt{Z_N(\vec{k})} \frac{C_+^{\mathcal{O}\bar{N}}(\vec{k},t)}{C_+^{N\bar{N}(\vec{k},t)}} \overset{t\to\infty}{=} f_N, \qquad (73)$$

where $Z_N(\vec{k})$ is obtained from two-state fits (36). These ratios are shown in Fig. 12 for both ensembles for $\vec{k}=0$. Although the proton decay constants can be extracted from correlators with any momentum $\vec{k}$, we study only zero-momentum ($\vec{k}=0$) data that has the highest statistical precision. We observe much less excited-state effects in the case of 32ID ensemble, which we attribute to oversmearing of quark sources on this ensemble. This oversmearing leads to stronger suppression of the excited states in the "smeared-point" correlator (73), while its statistical fluctuations are mostly cancelled in the combination with the "smeared-smeared" two-point function (28) and its parameter Z_N. We estimate the decay constant values from plateaus in the time range $5 \le t/a \le 8$ for the 24ID ensemble and $2 \le t/a \le 8$ for the 32ID ensemble.

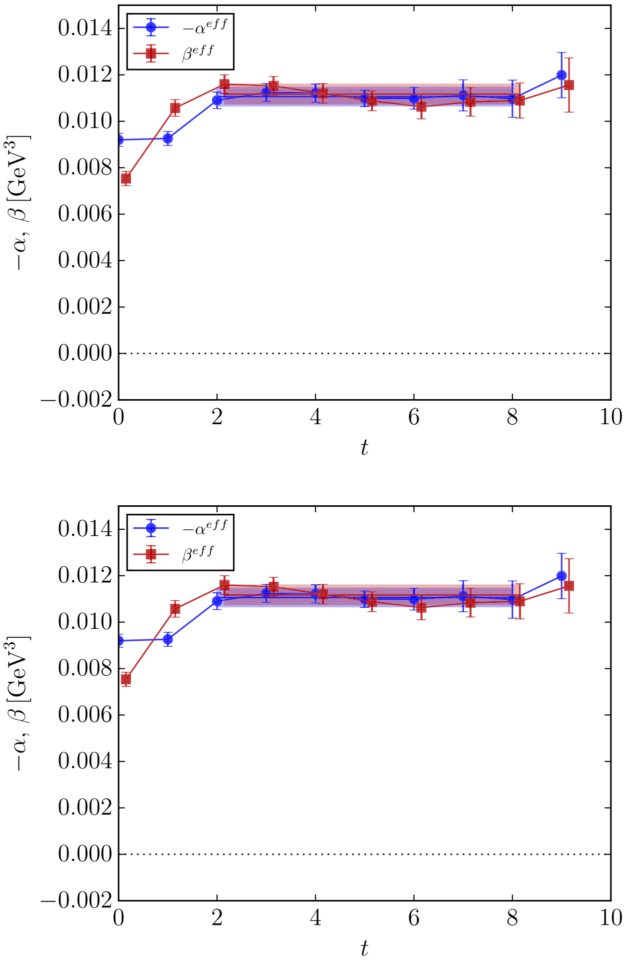

FIG. 12. Ratios (73) determining the proton decay constants ($-\alpha$) and β on 24ID (top) and 32ID (bottom) ensembles.

The proton decay constant results are collected in Table IX. Continuum extrapolations $\sim(f_N + f'_N a^2)$ of the proton decay constants α, β are shown in Fig. 13. Similarly to the proton decay amplitudes, uncertainties from the continuum extrapolation are estimated as the difference between the extrapolated results and the values on the finer 32ID ensemble. For both constants, the

TABLE IX. Results for the proton decay constants α, β on the two ensembles and in the continuum limit. The first uncertainty is statistical, the second is systematic due to the continuum extrapolation.

	24ID	32ID	Cont.
α	−0.0999(59)	−0.01106(39)	−0.01257(111)
β	0.01020(57)	0.01117(42)	0.01269(107)

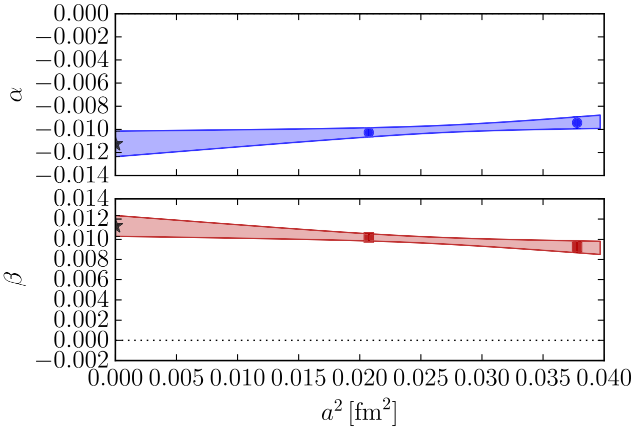

FIG. 13. Continuum $O(a^2)$ extrapolations of the proton decay constants $(-\alpha)$ and β.

statistical as well as systematic uncertainties from continuum extrapolation are roughly 10%, so that the total uncertainties are comparable to those in the direct determination of the proton decay form factors W_0.

V. DISCUSSION

The main finding of our paper is that proton decay amplitudes *are not suppressed* as the quark masses decrease and approach their physical values, and thus findings in previous lattice calculations (e.g., Ref. [42]) are valid. Using physical quark masses and absence of chiral extrapolation have resulted in a dramatic improvement of precision, yielding results that are perfectly consistent with those of Ref. [42]. Therefore, dynamical suppression of proton decay amplitudes due to nonperturbative QCD dynamics, as suggested in Ref. [33], is unlikely, at least at the physical u-,d-quark masses, and *the stringent constraints on the grand-unified Theories remain unchanged.*

In this work, we have used the $N_f = (2+1)$-flavor chirally-symmetric domain wall fermion action with physical quark masses on a lattice to compute transition matrix elements from proton to pion or kaon ("direct method"). We have omitted the η-channel decay amplitudes because they require evaluation of disconnected contractions to the two- and three-point functions, without which the results would be totally misleading at the physical point. Lattice calculations in this work have been performed in the exact isospin limit and without QED corrections, which is unlikely to introduce significant systematic bias compared to the current level of precision. Respective matrix elements for the neutron decays of which can also be potentially observed inside nuclei are related to those of the proton by isospin symmetry. Additionally, we have also calculated the proton (neutron) decay constants that can be used for computing rates of nonhadronic proton decays such as $p \to 3\ell$.

We have obtained proton decay form factors at the relevant kinematic points $Q^2 = -m_\ell^2$ by computing them at three small values of the lepton 4-momentum squared $|Q^2| \lesssim 0.15$ GeV^2 and performing linear interpolations. Form factor values are reported at the kinematic points with an electron and a muon in the final state, although the differences are insignificant. Our results are nonperturbatively renormalized using a variant of SMOM scheme suitable for our coarse lattice spacings and converted to the $\overline{\text{MS}}$ scheme using $O(\alpha_S^3)$ perturbative calculations, which is expected to have only negligible systematic uncertainties. We find no signs of mixing between operators constructed from chiral fermion fields; absence of such mixing indicates that chiral symmetry is preserved in our calculations.

We compare our results to earlier studies in Fig. 14, where we show results from direct and indirect calculations of the $p \to \pi\bar{\ell}$ and $p \to K\bar{\ell}$ proton decay amplitudes (assuming $m_\ell \approx 0$). Our results are in very good agreement with earlier direct calculations that used dynamical domain wall quark action at heavier pion masses [42]. Also, our results are in reasonable agreement with quenched

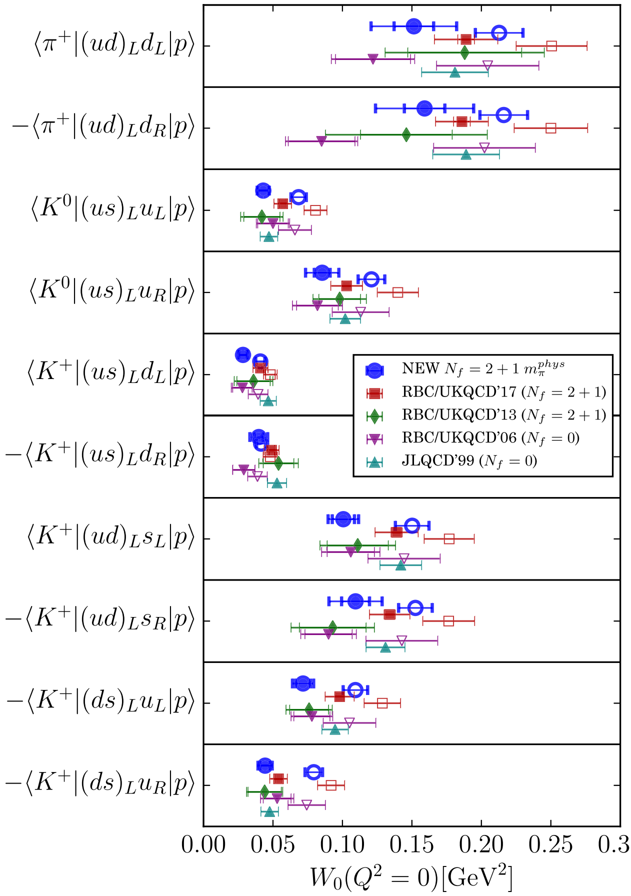

FIG. 14. Comparison of our results ("NEW") for the proton decay amplitudes $W_0(0)$ computed directly (filled symbols) and indirectly (open symbols) to previous determinations [38,40,42]. All results are renormalized to the $\overline{\text{MS}}$(2 GeV) scheme.

calculations that used domain wall [38] and Wilson [40] fermions. We have also found reasonable agreement of our indirect determination of the amplitudes with the analogous quenched results obtained earlier [38].

In comparison with the direct determination, the indirect determination have been found to yield results systematically higher in magnitude; similar pattern was observed in Ref. [38]. It is not a big surprise that there is difference between these two methods. First, the leading-order chiral perturbation theory should not be expected to produce precise results in general. Second, the final meson momenta are relatively high and the outgoing pion is not "soft". Since our results are obtained with physical quark masses, they may present a challenge to the ChPT-based phenomenology at relatively high momenta $|p| \approx 500$ MeV. It is important to calculate proton decay amplitudes using at least the next-to-leading order ChPT to carry out a valid comparison to the direct lattice QCD results.

The precision of our results can be improved with additional statistics to reduce the stochastic uncertainty, which would also help further constrain excited-stated effects and systematic errors associated with them. Although we generally observe nearly perfect agreement between fits and "plateaus", we opt to estimate excited-state effects in a very conservative fashion. For this reason, these effects dominate the total uncertainty in some instances. Further, since we used relatively long Euclidean time source-sink separations $(t_\Pi - t_N) = 1\dots 2\,\mathrm{fm}$, it is extremely unlikely that the true excited-state systematic effects exceed our estimates.

Finite-volume effects may contribute to systematic uncertainty because both our ensembles have similar lattice volume $\approx (4.6\ \mathrm{fm})^3$ that correspond to $m_\pi L \approx 3.3$. A naive estimate suggests that these effects are of the order of $e^{-m_\pi L} \approx = 0.04$ which is substantially below the combined quoted uncertainties in Table VIII. Until a study with a different physical volume is performed, it is impossible to estimate finite volume effects with better certainty. Another related issue may be thermal effects due to a disconnected "spectator" pion appearing from the heat bath. Although assessing such contributions also requires a study on a larger lattice, they should be suppressed even stronger than any finite-volume effects, since $L_t \geq 2L_x$ on the both ensembles.

The largest potential sources of systematic uncertainty are discretization effects. We use two ensembles with different, albeit coarse, values of the lattice spacing. Due to our improved gauge action and chirally symmetric fermion action, discretization effects must vanish as even powers of the lattice spacing $c_2 a^2 + c_4 a^4 + \cdots$. With two lattice spacings, only $O(a^2)$ effects can be evaluated and removed. Our results may be subject to the higher $O(a^4)$ discretization effects, which are impossible to control without additinoal calculations with different lattice spacings. Although we observe very good scaling of our results, indicating that discretization errors are generally small, we estimate our discretization uncertainties in a conservative fashion, which is robust unless there is significant cancellation between $O(a^2)$ and $O(a^4)$ or higher effects. However, such scaling violations are extremely unlikely since other observables computed on these lattices are consistent with calculations on finer lattices [43,56], and the hadron dispersion relations are accurately reproduced on both ensembles (see Figs. 7 and 8).

Despite conservative and likely overestimated systematic uncertainties, we have been able to determine the nucleon decay constants α, β and form factors $W_{0,1}$ with 10%–20% precision, including the stochastic uncertainty. This finding definitively excludes suppression of nucleon decay matrix elements at light quark masses, and thus removes the remaining systematic uncertainty in constraining some grand-unified theories and completely excluding others such as (SUSY) $SU(5)$.

ACKNOWLEDGMENTS

The authors would like to thank Christoph Lehner, Tom Blum, Eigo Shintani, Hooman Davoudiasl, and Robert Shrock for many useful discussions. During this work, S. S. and J. Y. were supported by the National Science Foundation under CAREER Grant No. PHY-1847893. S. S. has also been supported by the RHIC Physics Fellow Program of the RIKEN BNL Research Center. T. I. was supported through Brookhaven National Laboratory, the Laboratory Directed Research and Development (LDRD) Program No. 21-043, and by Program Development Fund No. NPP PD 19-025. P. B. acknowledges Wolfson Fellowship WM160035, an Alan Turing Fellowship, and STFC Grants No. ST/P000630/1, No. ST/M006530/1, No. ST/L000458/1, No. ST/K005790/1, No. ST/K005804/1, and No. ST/L000458/1. P. B., T. I., and A. S. have also been supported in part by the U.S. Department of Energy, Office of Science, Office of Nuclear Physics under the Contract No. DE-SC-0012704 (BNL). Y. A. acknowledges JSPS KAKENHI Grant No. 16K05320. The computations were performed using the Qlua software suite [72] with (z)Möbius solvers from the Grid library [73]. The gauge configurations and (z) Möbius eigenvectors have been generously provided by the RBC/UKQCD collaboration. Computations for this work were carried out on facilities of the USQCD Collaboration, which are funded by the Office of Science of the U.S. Department of Energy.

APPENDIX A: CONVENTIONS

In this section we summarize the conventions that clarify definitions of operators and matrix elements throughout the paper. The Euclidean γ-matrices we use, $\gamma_\mu = \gamma_\mu^\dagger$, satisfy the same relations as in, e.g., Ref. [74]. Positive-parity spinors are governed by the continuum limit of the lattice Dirac equation,

$$(i\not{p}+m)u(\vec{p})=0, \qquad \bar{u}(\vec{p})(i\not{p}+m)=0, \qquad \text{(A1)}$$

where $i\not{p}=-E(\vec{p})\gamma_4+i\vec{\gamma}\cdot\vec{p}$ and $E(p)=\sqrt{\vec{p}^2+m^2}$ is the on-shell energy, and the momentum states are defined in accordance with Eqs. (19), (27), and (28).

The charge-conjugated spinors

$$v^C=C^{-1}(\bar{v})^T, \qquad \bar{v}^C=-v^T C \qquad \text{(A2)}$$

satisfy equations

$$(i\not{p}-m)v^C(\vec{p})=0, \qquad \bar{v}^C(\vec{p})(i\not{p}-m)=0, \qquad \text{(A3)}$$

where the Euclidean charge-conjugation matrix $C=\gamma_2\gamma_4$ satisfies

$$C\gamma_\mu C^{-1}=-\gamma_\mu^T, \qquad C\sigma_{\mu\nu}C^{-1}=-\sigma_{\mu\nu}^T. \qquad \text{(A4)}$$

Throughout the paper, we use the relativistic normalization of the particle states and matrix elements, which is compatible with Eq. (2) and is is typical for these quantities (see, e.g., Ref. [42]) and

$$\langle N(\vec{k}',s')|N(\vec{k},s)\rangle=\sqrt{2E_{\vec{k}}}\,\delta^{(3)}(\vec{k}'-\vec{k})\delta^{s's}, \qquad \text{(A5)}$$

$$\langle \ell(\vec{q}',s')|\ell(\vec{q},s)\rangle=\sqrt{2E_{\vec{q}}}\,\delta^{(3)}(\vec{q}'-\vec{q})\delta^{s's}, \qquad \text{(A6)}$$

$$\langle \Pi(\vec{p}')|\Pi(\vec{p})\rangle=\sqrt{2E_{\vec{p}}}\,\delta^{(3)}(\vec{p}'-\vec{p}). \qquad \text{(A7)}$$

With this convention, the form factors $W_{0,1}$ (11) have mass dimension two, and the low-energy constants α,β (16) have dimension three.

APPENDIX B: PROTON DECAY AMPLITUDES IN ChPT

According to the chiral Lagrangian method [34,40], each decay matrix element can be calculated using the proton decay constants α, β as follows:

$$\langle\pi^+|(ud)_L d_L|p\rangle=\frac{\beta}{f}[1+D+F], \qquad \text{(B1)}$$

$$\langle\pi^+|(ud)_L d_R|p\rangle=\frac{\alpha}{f}[1+D+F], \qquad \text{(B2)}$$

$$\langle K^0|(us)_L u_L|p\rangle=\frac{\beta}{f}\left[1-(D-F)\frac{m_N}{m_B}\right], \qquad \text{(B3)}$$

$$\langle K^0|(us)_L u_R|p\rangle=-\frac{\alpha}{f}\left[1+(D-F)\frac{m_N}{m_B}\right], \qquad \text{(B4)}$$

$$\langle K^+|(us)_L d_L|p\rangle=\frac{\beta}{f}\left[\frac{2D}{3}\frac{m_N}{m_B}\right] \qquad \text{(B5)}$$

$$\langle K^+|(us)_L d_R|p\rangle=\frac{\alpha}{f}\left[\frac{2D}{3}\frac{m_N}{m_B}\right] \qquad \text{(B6)}$$

$$\langle K^+|(ud)_L s_L|p\rangle=\frac{\beta}{f}\left[1+\left(\frac{D}{3}+F\right)\frac{m_N}{m_B}\right], \qquad \text{(B7)}$$

$$\langle K^+|(ud)_L s_R|p\rangle=\frac{\alpha}{f}\left[1+\left(\frac{D}{3}+F\right)\frac{m_N}{m_B}\right], \qquad \text{(B8)}$$

$$\langle K^+|(ds)_L u_L|p\rangle=-\frac{\beta}{f}\left[1-\left(\frac{D}{3}-F\right)\frac{m_N}{m_B}\right], \qquad \text{(B9)}$$

$$\langle K^+|(ds)_L u_R|p\rangle=\frac{\alpha}{f}\left[1+\left(\frac{D}{3}-F\right)\frac{m_N}{m_B}\right], \qquad \text{(B10)}$$

where $D=0.8$, $F=0.47$, $m_N=0.94$ GeV, $m_B=1.15$ GeV, and $af=0.13055$.

APPENDIX C: PERTURBATIVE RENORMALIZATION

Throughout the paper, the uniform convention for renormalization factors of quark fields and operators is to convert from bare to renormalized quantities,

$$\mathcal{O}^R(\mu)=Z_{\mathcal{O}}^{R[\mathrm{reg}]}(\mu)\mathcal{O}^{[\mathrm{reg}]}, \qquad q^R(\mu)=\sqrt{Z_q^{R[\mathrm{reg}]}(\mu)}\,q^{[\mathrm{reg}]}, \qquad \text{(C1)}$$

where μ is the scale associated with the renormalization scheme R and "reg." is the regulator ϵ (dim.reg.) or a (lattice). The anomalous dimensions are defined as

$$\gamma_X=\frac{d\log Z_X}{d\log\mu} \qquad \text{(C2)}$$

for $X=\mathcal{O}$ or q. These conventions differ from some of the references.

To convert operators normalization from the $\mathrm{SMOM}_{\gamma_\mu}$/SYM3q to the $\overline{\mathrm{MS}}$ scheme, we use the $\overline{\mathrm{MS}}$-renormalized amputated Green's function of the three-quark operator with external quark fields with the SYM3q momenta $p^2=k^2=r^2=\mu^2$ [63]

$$[\Lambda_\pm^{\overline{\mathrm{MS}}}]_{\mathrm{SYM3q}}=1+0.989426\left(\frac{\alpha_S}{4\pi}\right) + (41.53105\mp1.69085-3.91418N_f)\left(\frac{\alpha_S}{4\pi}\right)^2. \qquad \text{(C3)}$$

The multiplicatively renormalized (diagonal) Green's functions (C3) are obtained for operators $\mathcal{O}_\pm=\mathcal{O}_{SS}^{3q}\pm\mathcal{O}_{PP}^{3q}$ with spin-color projectors $\Pi_\pm=\frac{1}{2}(\Pi_{SS}^{3q}\pm\Pi_{PP}^{3q})$, respectively [see Eq. (59)]. Since the quark field is also $\overline{\rm MS}$-renormalized in Eq. (C3), the difference from the lattice scheme for Z_q must be taken into account to get perturbative conversion factors for the three-quark operators,

$$\begin{aligned} C_{\pm}^{\overline{\rm MS}\leftarrow {\rm SMOM}_{\gamma_\mu}/{\rm SYM3q}} &= \left(\frac{Z_{\pm}^{\overline{\rm MS}}(|p|)}{Z_{\pm}^{{\rm SMOM}_{\gamma_\mu}/{\rm SYM3q}}(|p|)}\right) \\ &= [\Lambda_{\pm}^{\overline{\rm MS}}]_{\rm SYM3q}\cdot C_q^{\overline{\rm MS}\leftarrow {\rm SMOM}_{\gamma_\mu}}, \end{aligned} \tag{C4}$$

where the field conversion factor has been computed in Ref. [68]

$$\begin{aligned} C_q^{\overline{\rm MS}\leftarrow {\rm SMOM}_{\gamma_\mu}/{\rm SYM3q}} &= \left(\frac{Z_q^{\overline{\rm MS}}}{Z_q^{{\rm SMOM}_{\gamma_\mu}}}\right) = 1+\frac{4}{3}\left(\frac{\alpha_S}{4\pi}\right) \\ &\quad + (9.59901 + 0.185185 N_f)\left(\frac{\alpha_S}{4\pi}\right)^2. \end{aligned} \tag{C5}$$

Finally, the anomalous dimensions for operators $\mathcal{O}_{\pm}^{3q}$ are also provided in Ref. [63] to the $O(\alpha_S^3)$ order,

$$\begin{aligned} \gamma_{+}^{\overline{\rm MS}} &= -4\left(\frac{\alpha_S}{4\pi}\right) + \frac{2}{9}(-2N_f - 21)\left(\frac{\alpha_S}{4\pi}\right)^2 + \frac{1}{81}(260N_f^2 \\ &\quad + (4320\zeta_3 - 4740)N_f + 2592\zeta_3 + 22563)\left(\frac{\alpha_S}{4\pi}\right)^3, \end{aligned} \tag{C6}$$

$$\begin{aligned} \gamma_{-}^{\overline{\rm MS}} &= -4\left(\frac{\alpha_S}{4\pi}\right) + \frac{2}{9}(-2N_f - 81)\left(\frac{\alpha_S}{4\pi}\right)^2 + \frac{1}{81}(260N_f^2 \\ &\quad + (4320\zeta_3 - 4572)N_f + 24399)\left(\frac{\alpha_S}{4\pi}\right)^3. \end{aligned} \tag{C7}$$

---

[1] J. C. Pati and A. Salam, Unified lepton-hadron symmetry and a gauge theory of the basic interactions, Phys. Rev. D **8**, 1240 (1973).

[2] H. Georgi and S. L. Glashow, Unity of All Elementary Particle Forces, Phys. Rev. Lett. **32**, 438 (1974).

[3] H. Fritzsch and P. Minkowski, Unified interactions of leptons and hadrons, Ann. Phys. (N.Y.) **93**, 193 (1975).

[4] O. Espinosa, High-energy behavior of baryon and lepton number violating scattering amplitudes and breakdown of unitarity in the standard model, Nucl. Phys. **B343**, 310 (1990).

[5] J. Ambjorn, T. Askgaard, H. Porter, and M. E. Shaposhnikov, Sphaleron transitions and baryon asymmetry: A Numerical real time analysis, Nucl. Phys. **B353**, 346 (1991).

[6] A. Sakharov, Violation of *CP* invariance, c asymmetry, and baryon asymmetry of the universe, Pis'ma Zh. Eksp. Teor. Fiz. **5**, 32 (1967).

[7] M. Fukugita and T. Yanagida, Baryogenesis without grand unification, Phys. Lett. **174B**, 45 (1986).

[8] D.-G. Lee, R. N. Mohapatra, M. K. Parida, and M. Rani, Predictions for proton lifetime in minimal nonsupersymmetric SO(10) models: An update, Phys. Rev. D **51**, 229 (1995).

[9] J. Hisano, H. Murayama, and T. Yanagida, Nucleon decay in the minimal supersymmetric SU(5) grand unification, Nucl. Phys. **B402**, 46 (1993).

[10] H. Murayama and A. Pierce, Not even decoupling can save minimal supersymmetric SU(5), Phys. Rev. D **65**, 055009 (2002).

[11] M. Krishnaswamy, M. Menon, N. Mondal, V. Narasimham, B. Sreekantan, Y. Hayashi, N. Ito, S. Kawakami, and S. Miyake, Fully confined events indicative of proton decay in the kolar gold fields detector, Phys. Lett. B **115**, 349 (1982).

[12] G. Battistoni *et al.*, Fully contained events in the Mont Blanc nucleon decay detector, Phys. Lett. **118B**, 461 (1982).

[13] G. Deuzet *et al.* (Aachen-Orsay-Ecole Poly-Saclay-Wuppertal Collaboration), Search for proton decay in the frejus experiment, in *19th International Cosmic Ray Conference* (1985).

[14] P. Litchfield *et al.* (Soudan-2 Collaboration), First results from the Soudan-2 proton decay experiment, J. Phys. G **17**, S393 (1991).

[15] K. Hirata *et al.* (Kamiokande-II Collaboration), Experimental limits on nucleon lifetime for lepton + meson decay modes, Phys. Lett. B **220**, 308 (1989).

[16] C. McGrew *et al.*, Search for nucleon decay using the IMB-3 detector, Phys. Rev. D **59**, 052004 (1999).

[17] K. Abe *et al.* (Super-Kamiokande Collaboration), Search for proton decay via $p \to e^+\pi^0$ and $p \to \mu^+\pi^0$ in 0.31 megaton years exposure of the Super-Kamiokande water Cherenkov detector, Phys. Rev. D **95**, 012004 (2017).

[18] K. Abe *et al.* (Super-Kamiokande Collaboration), Search for proton decay via $p \to \nu K^+$ using 260 kiloton year data of Super-Kamiokande, Phys. Rev. D **90**, 072005 (2014).

[19] R. Acciarri *et al.* (DUNE Collaboration), Long-baseline neutrino facility (LBNF) and deep underground neutrino

experiment (DUNE): Conceptual design report, volume 4 The DUNE detectors at LBNF, arXiv:1601.02984.

[20] K. Abe *et al.* (Hyper-Kamiokande Collaboration), Hyper-kamiokande design report arXiv:1805.04163.

[21] K. Abe *et al.*, Letter of intent: The hyper-kamiokande experiment—detector design and physics potential—, arXiv:1109.3262.

[22] R. Acciarri *et al.* (DUNE Collaboration), Long-baseline neutrino facility (LBNF) and deep underground neutrino experiment (DUNE): Conceptual design report, volume 2: The physics program for DUNE at LBNF, arXiv:1512.06148.

[23] F. An *et al.* (JUNO Collaboration), Neutrino physics with JUNO, J. Phys. G **43**, 030401 (2016).

[24] S. Dimopoulos and H. Georgi, Softly broken supersymmetry and SU(5), Nucl. Phys. **B193**, 150 (1981).

[25] E. Witten, Dynamical breaking of supersymmetry, Nucl. Phys. **B188**, 513 (1981).

[26] V. Lucas and S. Raby, Nucleon decay in a realistic SO(10) SUSY GUT, Phys. Rev. D **55**, 6986 (1997).

[27] S. Weinberg, Baryon and Lepton Nonconserving Processes, Phys. Rev. Lett. **43**, 1566 (1979).

[28] F. Wilczek and A. Zee, Operator Analysis of Nucleon Decay, Phys. Rev. Lett. **43**, 1571 (1979).

[29] E. Rinaldi, S. Syritsyn, M. L. Wagman, M. I. Buchoff, C. Schroeder, and J. Wasem, Lattice QCD determination of neutron-antineutron matrix elements with physical quark masses, Phys. Rev. D **99**, 074510 (2019).

[30] M. Gavela, A. Le Yaouanc, L. Oliver, O. Pene, and J. Raynal, Calculation of proton decay in the nonrelativistic quark model, Phys. Rev. D **23**, 1580 (1981).

[31] O. Kaymakcalan, C.-H. Lo, and K. C. Wali, Chiral lagrangian for proton decay, Phys. Rev. D **29**, 1962 (1984).

[32] T. Okazaki and K. Fujii, An extended application of the bag model: The proton decay, Phys. Rev. D **27**, 188 (1983).

[33] A. Martin and G. C. Stavenga, Non-perturbative proton stability, Phys. Rev. D **85**, 095010 (2012).

[34] M. Claudson, M. B. Wise, and L. J. Hall, Chiral lagrangian for deep mine physics, Nucl. Phys. **B195**, 297 (1982).

[35] Y. Hara, S. Itoh, Y. Iwasaki, and T. Yoshie, Proton decay and lattice QCD, Phys. Rev. D **34**, 3399 (1986).

[36] K. Bowler, D. Daniel, T. Kieu, D. Richards, and C. Scott, Nucleon wave functions from lattice gauge theories: Measurements of baryonic operators, Nucl. Phys. **B296**, 431 (1988).

[37] N. Tsutsui *et al.* (*CP*-PACS and JLQCD Collaboration), Lattice QCD calculation of the proton decay matrix element in the continuum limit, Phys. Rev. D **70**, 111501 (2004).

[38] Y. Aoki, C. Dawson, J. Noaki, and A. Soni, Proton decay matrix elements with domain-wall fermions, Phys. Rev. D **75**, 014507 (2007).

[39] Y. Aoki, P. Boyle, P. Cooney, L. Del Debbio, R. Kenway, C. Maynard, A. Soni, and R. Tweedie (RBC-UKQCD Collaboration), Proton lifetime bounds from chirally symmetric lattice QCD, Phys. Rev. D **78**, 054505 (2008).

[40] S. Aoki *et al.* (JLQCD Collaboration), Nucleon decay matrix elements from lattice QCD, Phys. Rev. D **62**, 014506 (2000).

[41] Y. Aoki, E. Shintani, and A. Soni, Proton decay matrix elements on the lattice, Phys. Rev. D **89**, 014505 (2014).

[42] Y. Aoki, T. Izubuchi, E. Shintani, and A. Soni, Improved lattice computation of proton decay matrix elements, Phys. Rev. D **96**, 014506 (2017).

[43] T. Blum *et al.* (RBC and UKQCD Collaborations), Domain wall QCD with physical quark masses, Phys. Rev. D **93**, 074505 (2016).

[44] P. A. Boyle *et al.*, Low energy constants of SU(2) partially quenched chiral perturbation theory from $\mathrm{N}_f = 2 + 1$ domain wall QCD, Phys. Rev. D **93**, 054502 (2016).

[45] T. Blum, N. Christ, M. Hayakawa, T. Izubuchi, L. Jin, C. Jung, and C. Lehner, Hadronic Light-by-Light Scattering Contribution to the Muon Anomalous Magnetic Moment from Lattice QCD, Phys. Rev. Lett. **124**, 132002 (2020).

[46] D. Silverman and A. Soni, The decay proton $\rightarrow e^+\gamma$ in grand unified gauge theories, Phys. Lett. **100B**, 131 (1981).

[47] T. Hambye and J. Heeck, Proton Decay into Charged Leptons, Phys. Rev. Lett. **120**, 171801 (2018).

[48] S. Girmohanta and R. Shrock, Improved lower bounds on partial lifetimes for nucleon decay modes, Phys. Rev. D **100**, 115025 (2019).

[49] M. Tanaka *et al.* (Super-Kamiokande Collaboration), Search for proton decay into three charged leptons in 0.37 megaton-years exposure of the Super-Kamiokande, Phys. Rev. D **101**, 052011 (2020).

[50] D. G. Phillips II *et al.*, Neutron-antineutron oscillations: theoretical status and experimental prospects, Phys. Rep. **612**, 1 (2016).

[51] E. Rinaldi, S. Syritsyn, M. L. Wagman, M. I. Buchoff, C. Schroeder, and J. Wasem, Neutron-Antineutron Oscillations from Lattice QCD, Phys. Rev. Lett. **122**, 162001 (2019).

[52] L. Abbott and M. B. Wise, The effective Hamiltonian for nucleon decay, Phys. Rev. D **22**, 2208 (1980).

[53] R. Arthur *et al.* (RBC and UKQCD Collaborations), Domain wall QCD with near-physical pions, Phys. Rev. D **87**, 094514 (2013).

[54] D. Renfrew, T. Blum, N. Christ, R. Mawhinney, and P. Vranas, Controlling residual chiral symmetry breaking in domain wall fermion simulations, Proc. Sci., LATTICE2008 (**2008**) 048.

[55] D. Murthy, Precision light flavor physics from Lattice QCD, Ph.D. thesis, Columbia University, 2017.

[56] J. Tu, Lattice QCD simulations towards strong and weak coupling limits, Ph.D. thesis, Columbia University, 2020.

[57] T. Blum, T. Izubuchi, and E. Shintani, New class of variance-reduction techniques using lattice symmetries, Phys. Rev. D **88**, 094503 (2013).

[58] R. Brower, R. Babich, K. Orginos, C. Rebbi, D. Schaich *et al.*, Moebius algorithm for domain wall and GapDW fermions, Proc. Sci. LATTICE2008 (**2008**) 034.

[59] M. A. Clark, C. Jung, and C. Lehner, Multi-grid lanczos, in 35th International Symposium on Lattice Field Theory (Lattice 2017) Granada, Spain, 2017 (2017), arXiv:1710.06884.

[60] S. Gusken, A study of smearing techniques for hadron correlation functions, Nucl. Phys. B, Proc. Suppl. **17**, 361 (1990).

[61] G. Martinelli, C. Pittori, C. T. Sachrajda, M. Testa, and A. Vladikas, A general method for nonperturbative

renormalization of lattice operators, Nucl. Phys. **B445**, 81 (1995).

[62] C. Sturm, Y. Aoki, N. H. Christ, T. Izubuchi, C. T. C. Sachrajda, and A. Soni, Renormalization of quark bilinear operators in a momentum-subtraction scheme with a nonexceptional subtraction point, Phys. Rev. D **80**, 014501 (2009).

[63] J. Gracey, Three loop renormalization of 3-quark operators in QCD, J. High Energy Phys. 09 (2012) 052.

[64] Y. Aoki *et al.* (private communications).

[65] A. Pivovarov and L. Surguladze, Anomalous dimensions of octet baryonic currents in two loop approximation, Nucl. Phys. **B360**, 97 (1991).

[66] V. D. Barger and R. J. N. Phillips, Collider physics: 1993, arXiv:hep-ph/9309250.

[67] C. Alexandrou, M. Constantinou, and H. Panagopoulos (ETM Collaboration), Renormalization functions for $N_f = 2$ and $N_f = 4$ twisted mass fermions, Phys. Rev. D **95**, 034505 (2017).

[68] L. G. Almeida and C. Sturm, Two-loop matching factors for light quark masses and three-loop mass anomalous dimensions in the RI/SMOM schemes, Phys. Rev. D **82**, 054017 (2010).

[69] P. Zyla *et al.* (Particle Data Group), Review of particle physics, Prog. Theor. Exp. Phys. **2020**, 083C01 (2020).

[70] C. Kelly and T. Wang, Update on the improved lattice calculation of direct *CP*-violation in K decays, in *37th International Symposium on Lattice Field Theory (Lattice 2019) Wuhan, Hubei, China, 2019* (2019), arXiv:1911.04582.

[71] See Supplemental Material at http://link.aps.org/supplemental/10.1103/PhysRevD.105.074501 for form factor plateau and fit figures for all channels and ensembles.

[72] A. Pochinsky, Qlua lattice software suite, https://usqcd.lns.mit.edu/qlua (2008–present).

[73] P. Boyle *et al.*, Grid: Data parallel C++ mathematical object library, https://github.com/paboyle/Grid.

[74] M. Abramczyk, S. Aoki, T. Blum, T. Izubuchi, H. Ohki, and S. Syritsyn, Lattice calculation of electric dipole moments and form factors of the nucleon, Phys. Rev. D **96**, 014501 (2017).